Contents lists available at ScienceDirect

Materials Today Bio

"One-stop" synergistic strategy for hepatocellular carcinoma postoperative recurrence

Yiming Liu [a],[1], Chuan Tian [a],[b],[1], Chengzhi Zhang [a], Zaoqu Liu [a], Jing Li [a], Yahua Li [a], Quanhui Zhang [a], Shengnan Ma [c],[**], Dechao Jiao [a],[***], Xinwei Han [a],[****], Yanan Zhao [a],[*]

[a] *Department of Interventional Radiology, Key Laboratory of Interventional Radiology of Henan Province, The First Affiliated Hospital of Zhengzhou University, Zhengzhou, 450052, PR China*
[b] *Department of Interventional Medical Center, The Affiliated Hospital of Qingdao University, No. 1677 Wutaishan Road, Shandong, 266000, Qingdao, PR China*
[c] *Department of Endocrinology and Metabolism, The First Affiliated Hospital of Zhengzhou University, Zhengzhou, 450052, Henan, PR China*

ARTICLE INFO

ABSTRACT

Residual tumor recurrence after surgical resection of hepatocellular carcinoma (HCC) remains a considerable challenge that imperils the prognosis of patients. Notably, intraoperative bleeding and postoperative infection are potential risk factors for tumor recurrence. However, the biomaterial strategy for the above problems has rarely been reported. Herein, a series of cryogels (coded as SQ-n) based on sodium alginate (SA) and quaternized chitosan (QC) were synthesized and selected for optimal ratios. The *in vitro* assays showed that SQ-50 possessed superior hemostasis, excellent antibacterial property, and great cytocompatibility. Subsequently, SQAP was constructed by loading black phosphorus nanosheets (BPNSs) and anlotinib hydrochloride (AL3818) based on SQ-50. Physicochemical experiments confirmed that near-infrared (NIR)-assisted SQAP could control the release of AL3818 in photothermal response, significantly inhibiting the proliferation and survival of HUVECs and H22 cells. Furthermore, *in vivo* studies indicated that the NIR-assisted SQAP prevented local recurrence of ectopic HCC after surgical resection, achieved through the synergistic effect of mPTT and molecular targeted therapy. Thus, the multifunctional SQAP provides a "one-stop" synergistic strategy for HCC postoperative recurrence, showing great potential for clinical application.

1. Introduction

Hepatocellular carcinoma (HCC) is the most common type of liver cancer, accounting for 90% of all liver cancer cases [1–4]. Although surgical resection is the mainstream treatment for HCC [2], intraoperative bleeding [5,6], postoperative infection [7,8], and postoperative tumor recurrence [9,10] remain severe challenges in clinical practice. Traditional clinical strategies, including gauze for bleeding, antibiotics for infection, and radiotherapy and chemotherapy for tumor recurrence, do not achieve satisfactory effects [11]. Therefore, constructing a "one-stop" synergistic strategy to simultaneously address hemostasis, antibacterial resistance, and recurrence after surgical resection of HCC is urgent and promising.

The abundant blood supply in the liver and HCC makes intraoperative bleeding almost inevitable, with extremely rapid and incompressible [12]. Recently, various hemostatic materials, such as nanofibers [13], sponges [14], and hydrogels [14], have been designed for rapid hemostasis. Cryogels are obtained by temperatures below the normal freezing point of bulk solvents [15]. They are applied for rapid hemostasis by virtue of their large pore size, high porosity, and elastic texture resembling soft tissue [16]. Low immunogenic sodium alginate (SA) is a natural polysaccharide that has been widely used in the preparation of cryogels due to its transient physical cross-linking properties [17]. For instance, Wang et al. constructed the SA/PDA (polydopamine)

cryogels through one-step blending and freeze-thaw technology [18]. In addition, our previous studies have demonstrated that quaternized chitosan (QC) has superior hemostatic and Gram-positive/negative bacteria inhibition properties [19]. Cationic QC can cross-link with carboxyl-rich SA through electrostatic interactions to form stable SA/QC cryogels (SQ), which imparts hemostasis and antibacterial properties and can also be an ideal candidate as a drug delivery platform.

Theoretically, molecular targeted drugs that target downregulate aberrantly activated specific molecules in tumor cells are more specific for cancer cells than cytotoxic drugs that target cell replication [20,21]. He et al. [22] found that vascular endothelial growth factor A (VEGFA) expression is higher in HCC compared to normal tissue, and the VEGFA-vascular endothelial growth factor receptor (VEGFR) signaling pathway plays a vital role in tumor cell survival, proliferation, and angiogenesis [23]. As a novel multi-targeted receptor tyrosine kinase (RTK) inhibitor, anlotinib hydrochloride (AL3818) inhibits the RTK activity of VEGFR and blocks the phosphorylation of PI3K/AKT and MAPK/ERK signaling pathways downstream of VEGFR [22,24,25]. Further, AL3818 not only inhibits tumor angiogenesis but also inhibits tumor proliferation and survival [25]. However, the low solubility, poor bioavailability, and off-target activity of commercial oral AL3818 greatly limit its optimal efficacy [25,26]. Local administration using AL3818-loaded SQ seems to be a potential strategy, but molecular targeted therapy alone is not enough to achieve the goal of preventing tumor recurrence.

Recently, mild photothermal (mPTT, ≤48 °C) responsive drug delivery systems have been attracting widespread attention. In contrast to hyperthermic stimulation, mPTT induces heat stress responses such as protein and nucleic acid denaturation in tumor cells, leading to apoptosis [27]. Importantly, mPTT also protects the surrounding normal tissues from excessive thermal damage, especially the remaining liver tissue after resection of HCC [28]. Various photothermal agents, such as gold [29], platinum [30], phosphorus [31], and polydopamine [32], have been used in mPTT therap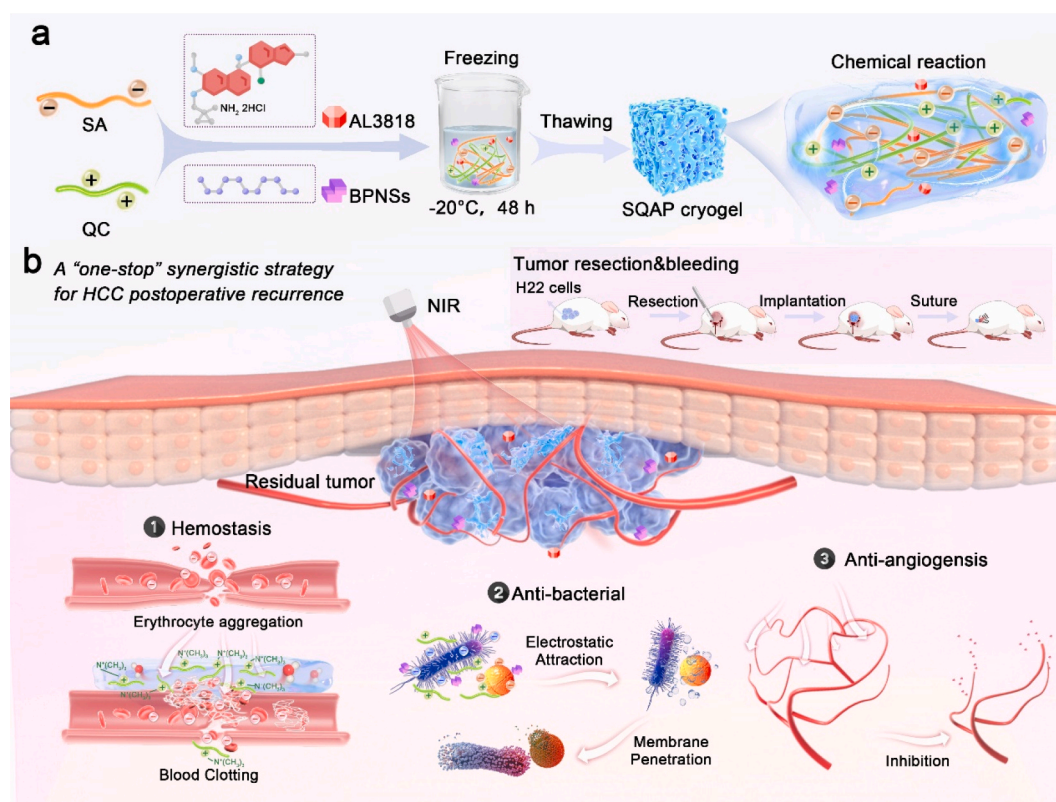y. Among them, black phosphorus nanosheets (BPNSs) are novel two-dimensional ultrathin layered inorganic materials with broad region light absorption, excellent photothermal conversion, and biocompatibility [33,34]. Inspired by this, we introduced AL3818 and BPNSs into SQ. By utilizing near-infrared (NIR) irradiation, BPNSs can not only effectively damage the residual tumor cells at the resection site through mPTT but also "on-demand" release AL3818 to achieve a synergistic anti-tumor recurrence effect.

Herein, we designed and synthesized a multifunctional cryogel based on SA, QC, BPNSs, and AL3818 for intraoperative hemostasis, postoperative anti-infection, and anti-tumor recurrence *in situ*. As shown in Scheme 1 a series of SQ-n were fabricated to select the most suitable ratio, and SQ-50 was chosen to construct SQAP due to its excellent physicochemical, hemostatic, antimicrobial, and biocompatible properties. Subsequently, the SQAP was transplanted to the ectopic HCC surgical resection site in mice to evaluate its antitumor recurrence effect. First, SQAP with a porous structure can quickly stop bleeding, and its positively charged QC component also promotes the aggregation of negatively charged red blood cells to form blood clots, achieving rapid hemostasis. Second, the QC component in SQAP absorbs the negatively charged bacteria and disrupts the bacterial membrane, playing a broad-spectrum antibacterial role. More importantly, NIR-assisted BPNSs convert light energy into heat energy, exerting mPTT effects while controlling the release of AL3818, which effectively restrains abnormal tumor angiogenesis and suppresses tumor recurrence. Overall, the multifunctional SQAP provides a "one-stop" synergistic strategy for HCC postoperative recurrence.

2. Methods and materials

2.1. Materials

QC (degree of substitution of 92%) and SA (Mw = 320 kDa) were purchased from Macklin Biochemical Co. Ltd. (Shanghai, China). BPNSs

Scheme 1. Schematic illustration of the SQAP carrying anlotinib hydrochloride (AL3818) and black phosphorus nanosheets (BPNSs) with the assistance of NIR irradiation for HCC postoperative recurrence.

(0.8 mg/mL in ethanol) were provided by Nanjing XFNANO Mater. Tech. Co. Ltd. (Nanjing, China). AL3818 was supplied by Nanjing Zhengda Tianqing Pharmaceutical Co., Ltd (Nanjing, China). Mouse Hepatoma-22 (H22) and Human umbilical vein endothelial cells (HUVECs) were obtained from the Shanghai Cell Center (Chinese Academy of Sciences). RPIM-1640 (1640, PM150110), medium Dulbecco's modified Eagle's medium (DMEM, PM150210), fetal bovine serum (FBS, 164210), penicillin-streptomycin (PB180120), and trypsin-EDTA (PB180220) were supplied by Procell Life Science&Technology Co., Ltd. (Wuhan, China). Cell Counting Kit-8 (CCK-8, CK04) was obtained from Dojindo China Co., Ltd. (Shanghai, China). Live and Dead Cell Double Staining Kit (KTA1001) and Annexin V-AbFluor™ 488/PI Apoptosis Detection kit (KTA0002) were purchased from Abbkine Scientific Co., Ltd. (China, Wuhan). The Bacterial viability/virulence test kit (L6060S) was purchased from Shanghai BioScience Co., Ltd. (Shanghai, China). Other chemical and biological reagents were of analytical grade and were used without modification.

2.2. Preparation of the cryogels

Firstly, 2 wt% QC solution was prepared by dissolving 2 g of QC into deionized water. 2 wt% SA solution was prepared by dissolving 2 g of SA into deionized water. Then, QC and SA solutions were mixed in different proportions, and $CaCl_2$ (1 M) was added. After standing molding, a series of cryogels were obtained by freeze-drying, named SQ-n (n = 0, 30, 50, and 70, n representing QC content), where S represented SA and Q represented QC. After a series of in vitro evaluation tests, SQ-50 was selected as the substrate, and 1% AL3818 (Fig. S4) was added to prepare SQA according to the above steps. In addition, SQAP was prepared by adding 1% AL3818 and 0.5% BPNSs simultaneously, in which A represented AL3818 and P represented BPNSs (Table S1). Place the resultant samples in the dryer for later use.

2.3. Physicochemical characterization

The chemical structure of the cryogels was characterized by analyzing functional group vibrations by Fourier transform infrared (FTIR, TNZ1-5700, Nicolet, USA) at 400-4000 cm^{-1}. The chemical bond vibrations were tested by Raman spectroscopy (RAMANforce, Nanophoton, Japan) at 100-3600 cm^{-1}. The surface morphology and elemental composition of the cryogels were analyzed by scanning electron microscopy (SEM, JSM-7401F, JEOL, Japan) coupled with an energy dispersive spectroscopy (EDS) analysis system. The dry cylindrical SQ-n (10 mm × 10 mm, diameter × height) was immersed in water/rabbit whole blood and weighed at a fixed time to detect its water/blood absorption rate. The mechanical properties of the cryogels were tested by compression test at room temperature using an electronic universal testing machine (CMT6503; Shenzhen SANS Test Machine, China). Briefly, the cryogels were fabricated as cylindrical shapes with a diameter of 6 mm and a height of 3 mm. The cryogels were first subjected to compression tests at a strain rate of 2 mm/min, with a maximum compressive strain of 80%.

2.4. In vitro photothermal performance

To evaluate the photothermal conversion performance of the cryogels, SQA and SQAP were irradiated by 808 nm NIR with 0.5 and 0.8 W/cm^2 for 4 min, respectively. The SQAP was subjected to four NIR irradiation heating (808 nm, 0.8 W/cm^2, 2 min) and free cooling cycles to evaluate their photothermal stability. All temperature changes during this period were monitored in real-time by the Testo 865 infrared thermal imager (Testo Instruments International Trading Co., Ltd., Shanghai, China).

2.5. In vitro drug release behavior

For in vitro drug release behavior, SQA and SQAP were immersed in 5 mL of PBS and exposed to room temperature (RT), 808 nm NIR with 0.5 and 0.8 W/cm^2, respectively. The suspension was kept under shaking at 50 rpm. At predetermined time intervals, 1.0 mL of the release solution was collected for analysis, and 1.0 mL of fresh PBS was added to the extraction bottles. At various time points (0–14 d), the amount of released AL3818 was examined by graphite-furnace atomic absorption spectrometry (GF-AAS, Avanta M, GBC Scientific Equipment). To verify the controlled release of AL3818 by photothermal conversion of BPNSs, SQAP was immersed into PBS and exposed to 808 nm NIR with 0.5 and 0.8 W/cm^2 for 10 min at 8 h intervals, and the amount of released AL3818 was examined by graphite-furnace atomic absorption spectrometry over 24 h.

2.6. Biocompatibility evaluation

2.6.1. Hemolysis ratio test

For the hemolysis ratio test, fresh whole blood was extracted from rabbit hearts and diluted with saline at a ratio of 1:1.25. The SQ-n was subsequently co-incubated with the diluted blood at 37 °C for 1 h. The hemolysis status was observed after centrifugation at 3000 rpm for 10 min. The optical density (OD) at 545 nm of the supernatant was measured using a microplate analyzer (NanoDrop, Thermo Fisher, USA). The hemolysis ratio (HR) was calculated by the following equation: HR (%) = (ODs-ODn)/(ODp-ODn) × 100%. ODs, the OD values of the sample; ODp, the OD values of the positive control; and ODn, the OD values of the negative control.

2.6.2. Live/dead cell staining

Cell viability test was assessed by the Live and Dead Cell Double Staining Kit. L929 (5 × 10^4/mL) was inoculated in 24-well plates and incubated overnight. A total of 5 groups were divided: blank control (B. C.), SQ-0, SQ-30, SQ-50, and SQ-70 groups, that is, PBS or SQ-n extraction solutions and complete medium were added to each well, respectively, and further incubated for 24 h. Subsequently, the cells were washed with PBS, stained with Calcine-AM and propidium iodide (PI) for 20 min, and finally photographed under a fluorescence microscope (Carl Zeiss, Germany) and analyzed by Image J (National Institutes of Health, Bethesda, USA) for the number of live/dead L929 cells.

2.6.3. CCK-8 assay

Cell proliferation test was assessed by the CCK-8 Kit. L929 (1 × 10^3/mL) was inoculated in 96-well plates overnight. Subsequently, PBS or SQ-n extraction solutions were added to each well, as previously described. At 1, 2, and 3 days, CCK-8 reagent was added to each well and further incubated for another 3 h for color development. The OD at 450 nm was determined with a microplate reader. The relative cell proliferation rate was calculated by the following equation: Relative cell proliferation rate = [(ODc-ODs)/(ODc-ODb)] × 100%. ODb, the OD values of blank wells; ODc, the OD values of the control group on day 1; and ODs, the OD values of the samples group each day.

2.7. In vivo hemostatic effect

To evaluate the hemostatic effect of cryogels, the mouse tail amputation (MouTa), mouse partial hepatectomy (MouLi), and rabbit partial hepatectomy (RabLi) were constructed for comprehensive analysis. New Zealand rabbits (weighing 1.8–2.3 kg, females) and mice (weighing 18–22 g, females) were obtained from the laboratory animal center of Hualan Biological Co., Ltd (Henan, China). These animals were randomly divided into six groups: B.C., positive control (P·C.), SQ-0, SQ-30, SQ-50, and SQ-70 group. No treatment factors were imposed in the B.C. group. Commercial gauze was used as a treatment factor for the P.C.

group. The cryogels were placed on the wound of each animal model for the experiment. The blood loss and hemostasis time were recorded. Please refer to the supplementary materials for detailed protocols.

2.8. In vitro antibacterial activity

In this section, Methicillin-resistant Staphylococcus aureus (MRSA, ATCC 33592) and Escherichia coli (E. coli, ATCC 25922) was employed to test the antibacterial activity of cryogels. There were six groups: B.C., P·C., SQ-0, SQ-30, SQ-50, and SQ-70 groups. SQ-n were exposed to 30 min under ultraviolet (UV) light for sterilization and subsequent assays. Bacterial proliferation assay, clone formation assay, and live/dead bacterial staining assay were used to assess the survival and proliferation capacity of the treated bacteria. Please refer to the supplementary materials for detailed protocols.

2.9. In vitro anti-angiogenesis and anti-tumor effects

In this section, HUVECs and H22 cells were used to verify the anti-angiogenesis and anti-tumor effect of cryogels. Four groups included the B.C, SQA, SQAP, and SQAP + NIR groups. PBS, SQA, and SQAP extraction solutions were irradiated with UV light for 30 min to ensure sterility. In addition, the anti-tumor effect was also evaluated in the SQP + NIR group.

2.9.1. Live/dead cell staining and CCK8 assay
The effect of cryogels on cell activity and cell proliferation of HUVECs or H22 cells was assessed by live/dead cell staining and CCK-8 assay, respectively, as described in previous studies [19,35].

2.9.2. Cell apoptosis assay
Cryogels of each group were respectively co-incubated with HUVECs or H22 cells (3×10^5/mL) at 37 °C, washed with PBS, trypsin digested into single cell suspensions, stained with Annexin V-AbFluor™ 488 and PI for 20 min in dark, and then detected by flow cytometry (NOVO-CYte3130, ACEA, America).

2.9.3. Wound healing assay
HUVECs or H22 cells (1×10^5/mL) were inoculated into the 6-well plates. After forming a cell monolayer, a scratch was made with a sterile P200 pipette tip, and free cells were removed by rinsing with PBS. Subsequently, the corresponding treatment factors were added to each well in the different groups. Photographs of HUVECs and H22 cells were taken under light microscopy at 0 and 24 h, respectively. The wound healing rates were calculated by the following formula: Wound healing rate = (W0–W24)/W0 × 100%. W0, wound area at 0 h; W24, wound area at 24 h.

2.9.4. Transwell assay
HUVECs or H22 cells (5×10^4/mL) were inoculated into the upper chamber. Subsequently, the corresponding treatment factors were added to the upper chamber in the different groups. After co-incubation for 36 h, migrating cells retained on the upper surface of the filter membrane were removed with a cotton swab. The migrating cells on the lower surface of the filter membrane were stained with 0.5% crystal violet solution, fixed in 4% paraformaldehyde, and photographed under light microscopy. The number of migrated cells in each group was statistically analyzed using Image J software.

2.9.5. Tube formation assay
Firstly, 200 μL of Matrigel (BD Biosciences, Franklin Lakes, NJ, USA) per well was added to the lower chamber of pre-cooled 24-well plates and polymerized for 30 min at 37 °C. Then, a suspension of HUVECs (2 × 10^4/mL) was inoculated on the matrix gel. Subsequently, the corresponding treatment factors were added to each well in the different groups. After 6 h, cells were stained with Calcineurin-AM and

photographed under a fluorescence microscope. The branching points and capillary length of capillary-like structures were statistically analyzed using Image J software.

2.9.6. Immunofluorescence staining
To analyze the expression of TUNEL in H22 cells and CD31 in HUVECs, H22 cells or HUVECs were incubated on coverslips, treated with different factors for 1 d, fixed in 4% paraformaldehyde solution, and treated with 0.1% Triton X-100, respectively. The cells were then blocked with goat serum at 25 °C for 0.5 h. The H22 cells were incubated with an anti-TUNEL primary antibody, the HUVECs were incubated with an anti-CD31 primary antibody, and all groups of samples were incubated with FITC-labeled or Cy3-labeled secondary antibody (Tables S2–3). Cell nuclei were stained with DAPI. A microscope (IX53, Olympus, Japan) was used for data acquisition, and Image-Pro Plus software (Media Cybernetics, Silver Spring, MD, USA) was used for data analysis.

2.10. In vivo prevention of tumor recurrence by SQAP

To evaluate the effect of SQAP in preventing tumor recurrence after HCC resection in vivo, female Balb/C mice (4 weeks old) were purchased from the laboratory animal center of Hualan Biological Co., Ltd for the subsequent studies. All animals were raised in the Henan Provincial Animal Experiment Center (SPF sterile grade) and supplied daily water and feed to keep the mice healthy.

2.10.1. Ectopic HCC recurrence animal model
To establish the ectopic HCC recurrence animal model, 100 μL of PBS containing 5×10^6 resuspended H22 cells was injected into the right anterior dorsal side of Balb/C mice. Surgical resection of all visible tumors was performed when the tumor size reached 150 mm³, and this day was defined as day 0. Intraoperative hemostasis was performed using untreated, gauze, gelatin sponge (GS), and SQAP, and blood loss during surgical resection of tumors was recorded and further analyzed. Mice were randomly divided into four groups (n = 5) immediately after surgical resection: (1) no postoperative treatment (B.C. group); (2) saline containing AL3818 (5.0 mg/kg) was orally fed every 3 days starting from the postoperative 2nd day for a total of 5 times (AL3818 group); (3) SQAP were implanted at the resection site (SQAP group); (4) SQAP were implanted at the resection site, followed by NIR irradiation (0.8 W/cm², 5 min) every 3 days starting from the postoperative 2nd day for a total of 5 times (SQAP + NIR group). From Day 0, the body weights and tumor volumes of mice were monitored and analyzed. Considering the biodegradability of SQAP, it is unnecessary to remove them by secondary surgery, and they remained at the tumor resection site at the end of the mPTT cycles. On day 21, the mice were euthanized after removing the recurrent tumors under anesthesia.

2.10.2. In vivo photothermal performance
A better 808 nm NIR with 0.8 W/cm² was selected for in vivo evaluation based on the in vitro photothermal performance test results. NIR irradiation was respectively given to mice in the B.C., AL3818, and SQAP + NIR group at the time of the first postoperative NIR treatment. The data of temperature change were recorded in the same way as before.

2.10.3. In vivo ultrasound imaging
Before removing the recurrent tumors on day 21, ultrasound imaging was performed at the tumor resection sites of all mice in each group. B-mode ultrasound (Aplio 500, TOSHIBA, Japan) was used to detect the sizes of recurrent tumors, and Color Doppler (Aplio 500, TOSHIBA, Japan) was used to detect blood flow within the recurrent tumors.

2.10.4. Histological analysis
After the euthanasia of mice on day 21, tumor tissues were collected, fixed in 4% paraformaldehyde, paraffin-embedded, and sectioned.

Subsequently, H&E staining, immunofluorescence staining (labeling TUNEL, CD31, and HIF-1α), and immunohistochemical staining (labeling Ki67, VEGF, IL-6, and IL-10) were performed according to the corresponding standard procedures (Tables S2–3). The histological changes were observed under the microscope, and the expression of each observed index was analyzed by Image-Pro Plus software. Moreover, the heart, liver, spleen, lung, and kidney in mice of each group were collected and stained with H&E to assess the histocompatibility *in vivo*.

2.10.5. Animal survival test

The ectopic HCC recurrence model was established as described above; mice after surgical resection (recorded as day 0) were randomly divided into the same four groups: B.C., AL3818, SQAP, and SQAP + NIR group (n = 5). After treatment based on the same method as described above, the observation lasted until Day 40 to evaluate the overall survival rate of the mice.

2.10.6. In vivo degradation assay of SQAP

To investigate the retention time of biodegradable SQAP *in vivo*, the SQAP was transplanted into the subcutaneous tissue of Balb/c mice. At different time points after euthanasia (days 3, 7, 14, and 28), the SQAP and its surrounding tissues were removed, and H&E staining was conducted to observe the degradation of SQAP.

2.11. Statistical analysis

In this study, no less than three parallel groups were included in each experiment, and the data obtained were expressed as mean ± standard deviation. Independent samples *t*-test was used to analyze the differences between the two groups, one-way ANOVA was used to analyze the differences between multiple groups, and Kaplan-Meier (log-rank test) analysis was used to analyze the overall survival. All statistical analyses were carried out with GraphPad Prism 8.0, and a $P < 0.05$ was used to determine whether there was a significant difference (N·S., no significance; $*P < 0.05$; $**P < 0.01$; and $***P < 0.001$).

3. Results

3.1. Preparation of SQ-n

To endow the best performance to the cryogels, a series of SQ-n (SQ-0, 30, 50, and 70) based on SA and QC were firstly prepared. As shown in Fig. 1a, the FTIR of SA showed two strong absorption peaks at 1623 and 1417 cm^{-1} due to the asymmetric and symmetric vibrations of the carboxyl group along the alginate chain, respectively [36]. The C–H stretching vibration (1484 cm^{-1}) of CH$_3$ at the quaternary ammonium group, and the C=O stretching vibration (1650 cm^{-1}, amide I) and N–H stretching vibration (1562 cm^{-1}, amide II) of the amide group were presented in QC (Fig. 1b) [37]. In Fig. 1c, after the introduction of QC in SA, SQ-n could be distinguished by two strong absorption peaks by the carboxyl group (1631 cm^{-1}) vibrating along the alginate chain and the C–H stretching vibration (1478 cm^{-1}) of –N(CH$_3$)$_3^+$, respectively [38]. Meanwhile, it can be observed that the characteristic peaks of carboxyl and quaternary ammonium groups were shifted with the increase of QC ratio, and the amide group was masked by carboxylic acid on FTIR of SQ-n.

The Raman spectra were shown as a supplement in Fig. 1d–f. The characteristic peaks at 812, 891, and 960 cm^{-1} were from the backbone vibrations of SA, and the characteristic peaks at $\geq$ 1300 cm^{-1} were attributed to the stretching vibrations of the carboxyl group in SA [39]. The stretching vibrations of δ (CH$_2$) and δ (CH$_3$) of the QC were displayed at 1374 cm^{-1} and 1451 cm^{-1}, respectively (Fig. 1d) [40]. Fig. 1e presents an SQ-n Raman diagram. It can be seen that with the increase of QC content, the peak intensity of SQ-n increases significantly in the range of 750–1750 cm^{-1} and 2750-3500 cm^{-1}. In addition, we enlarged the dotted box to obtain Fig. 1f. Fig. 1f clearly shows the displacement of the characteristic peaks of SA and QC in SQ-30, SQ-50, and SQ-70. This

phenomenon could be attributed to strong electrostatic interactions between the quaternary ammonium cation of QC and the carboxylate anion of SA. Fig. 1e showed that, except for SQ-0, the characteristic peaks of SA and QC existed on SQ-30, 50, and 70. This result further validated the successful preparation of SQ-n.

Next, the microstructure and morphology of the SQ-n were observed by SEM (Fig. 1g). The SQ-0 had a connected macropore structure with smooth pore walls and high porosity (473.51 ± 51.18 μm). However, the pore walls gradually roughened with the increase in QC composition. The pore size also decreased to 107.22 ± 42.20 μm for SQ-50 and 62.76 ± 26.80 μm for SQ-70 (Fig. 1h). The water absorption ratio (Fig. 1i, Fig. S1) revealed that all the SQ-n were able to absorb water rapidly within 2 min and reached equilibrium within 15 min. With increasing QC content, the water absorption ratio decreased from 41.42 ± 2.18% of SQ-0 to 34.13 ± 2.73% of SQ-70. This may be related to pore size and the fact that QC is inherently less absorbent than SA. To better simulate the internal environment, we further soaked SQ-n in the rabbit whole blood for 1 min to explore the blood absorption ratio. Fig. 1j found that the blood absorption of SQ-n could reach more than 10% within 1 min, effectively addressing the problem of massive blood seepage during tumor resection.

3.2. Hemostatic, antibacterial, and biocompatibility performance of SQ-n

Since the risk of bleeding during surgical resection for HCC is extremely high, excellent hemostasis is important for cryogels. First, we co-incubated SQ-n with erythrocytes, and the results showed that the hemolysis rate of SQ-n was lower than 5%, and it would not cause the erythrocyte rupture (Fig. S2). The SEM results of erythrocytes co-incubated with SQ-50 showed that the erythrocyte presented a double-sided, slightly concave disk shape, further verifying that SQ-n would not destroy the erythrocyte membrane.

As shown in Fig. 2a–c, a MouTa model, a MouLi model, and a RabLi mode were used to assess the hemostatic effect of SQ-n. For the RabLi model, the blood loss and hemostasis time of SQ-50 and SQ-70 were reduced to 1.03 ± 0.16 g and 145.67 ± 10.02 s, and 0.78 ± 0.10 g and 121.33 ± 16.50 s, respectively, with significant differences, compared to other groups (Fig. 2d and e). Blood loss and hemostasis time in MouLi showed the same trend as in the RabLi model. The results showed that SQ-n exhibited significant hemostatic effects with increasing QC composition. The possible reasons for the excellent hemostatic properties of SQ-n are as follows: (1) QC activates exogenous and endogenous coagulation pathways in the organism [41]; (2) The positively charged quaternary ammonium group in QC can adsorb and aggregate negatively charged erythrocyte to rapidly form a blood clot [42]; (3) The cryogels rapidly absorbs water from the blood, thereby accelerating blood clotting and promoting hemostasis.

Postoperative infection following surgical resection of HCC is also a matter of concern. As shown in Fig. 2f, *E. coli* and MRSA were selected as representative bacteria to evaluate the antibacterial activity of SQ-n, respectively. The live/dead bacteria staining results showed that both *E. coli* and MRSA were utterly dead in the SQ-50 and SQ-70 groups. Moreover, as in the bacterial proliferation curve in Fig. 2g, the SQ-30, especially SQ-50, and SQ-70, resulted in a significant decrease in OD600 values of bacteria, indicating that QC can effectively inhibit the proliferation of bacteria. Fig. 2h and i shows bacterial culture plates, compared with the B.C. and SQ-0 group filled with bacteria, the SQ-n (n = 30, 50, and 70) significantly decreased the survival of *E. coli* and MRSA on the plates, from 87.09 ± 0.03% and 37.52 ± 0.08% for SQ-30 to 98.94 ± 0.01% and 90.03 ± 0.02% for SQ-50, and even 99.06 ± 0.00% and 91.14 ± 0.01% for SQ-70, respectively. This excellent antibacterial performance may be attributed to the fact that the positively charged amino and quaternary ammonium groups of QC in SQ-n can electrostatically adhere to the bacteria and disrupt the bacterial wall, leading to leakage of cytoplasmic constituents and cell death [43]. It is worth noting that SQ-n has a higher inhibitory effect on *E. coli* than
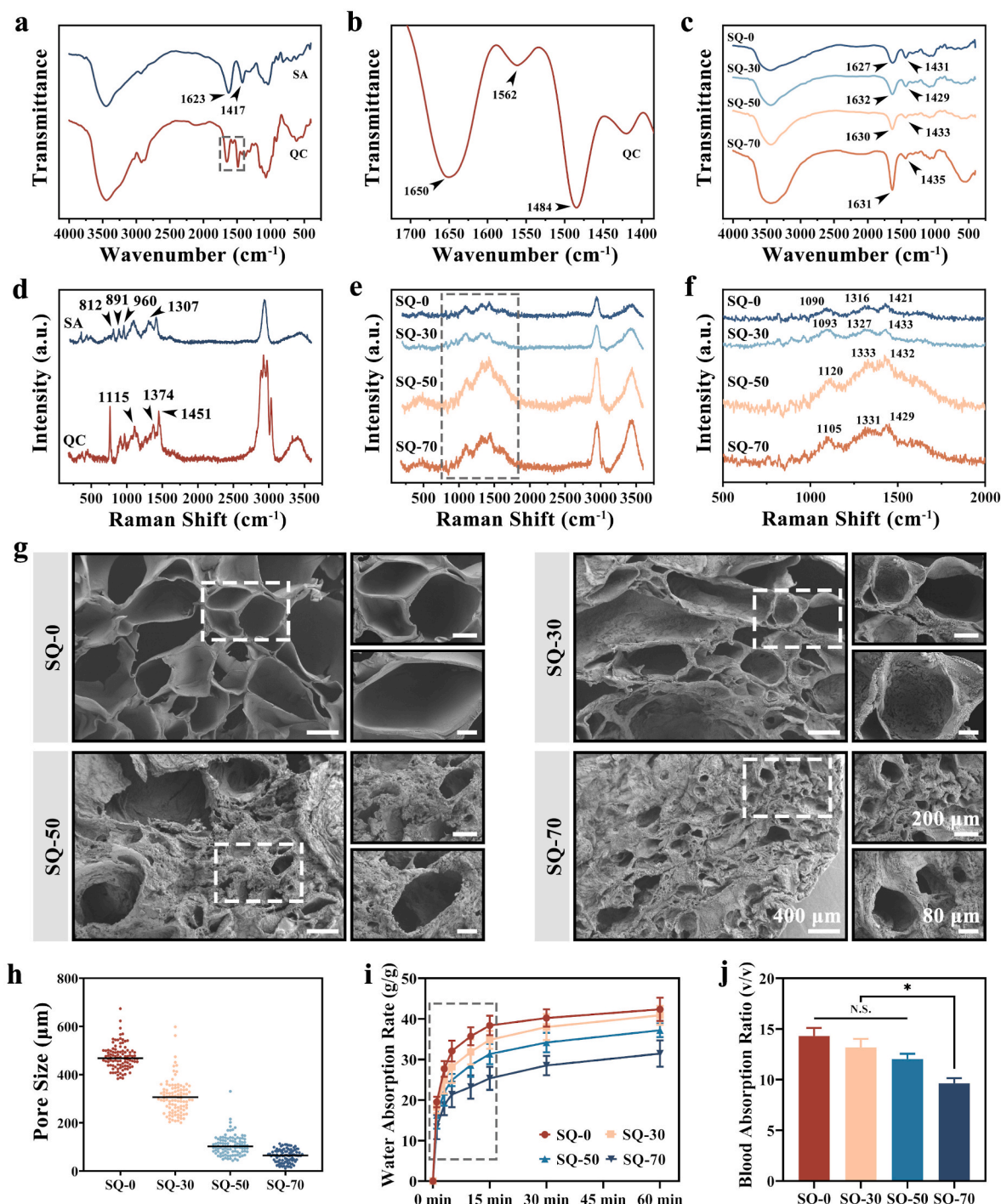
Fig. 1. Preparation and physicochemical characterization of SQ-n. (a–c) FTIR spectroscopy of SA and QC raw materials, amplification of FTIR characteristic peaks of QC, and FTIR spectroscopy of SQ-n. (d–e) Raman spectroscopy of SA and QC raw materials, and SQ-n. (f) Enlarged view of Raman spectrum of SQ-n. (g–h) SEM of SQ-n and pore size analysis. (i) Water absorption ratio, and (j) blood absorption ratio of SQ-n. Scale bar: 80 μm, 200 μm, and 400 μm.

MRSA. The reason is that (1) the negative charge on the surface of Gram-negative bacteria (*E. coli*) is higher than that of Gram-positive bacteria (MRSA), resulting in more adsorption of QC and higher inhibition of Gram-negative bacteria [44,45]. (2) Compared with *E. coli*, MRSA has a broader antimicrobial agent resistance by producing a large amount of penicillin-binding protein 2A, changing the antibiotic action target, producing modifying enzymes, and reducing membrane permeability [46].

Biocompatibility is the most essential and fundamental requirement for biomaterials directly applied to the human body. As shown in Fig. S1,

the quantitative analysis showed that the HR was significantly lower than 5%, indicating that SQ-n does not cause erythrocyte membrane rupture and has great hemocompatibility. Subsequently, L929 was used to assess the cytocompatibility and the ability to promote cell proliferation of SQ-n. The live/dead cell staining assays (Fig. S3a–b) showed that most L929 cells in the SQ-50 group survived (green), while some dead cells (red) were observed in the SQ-70 group. This result suggested that the higher QC in SQ-70 led to cytotoxicity. In addition, we further evaluated the effect of SQ-n on the proliferation of L929 cells by CCK8 assay (Fig. S3c). After 1–2 d of co-culture, the SQ-n groups exhibited
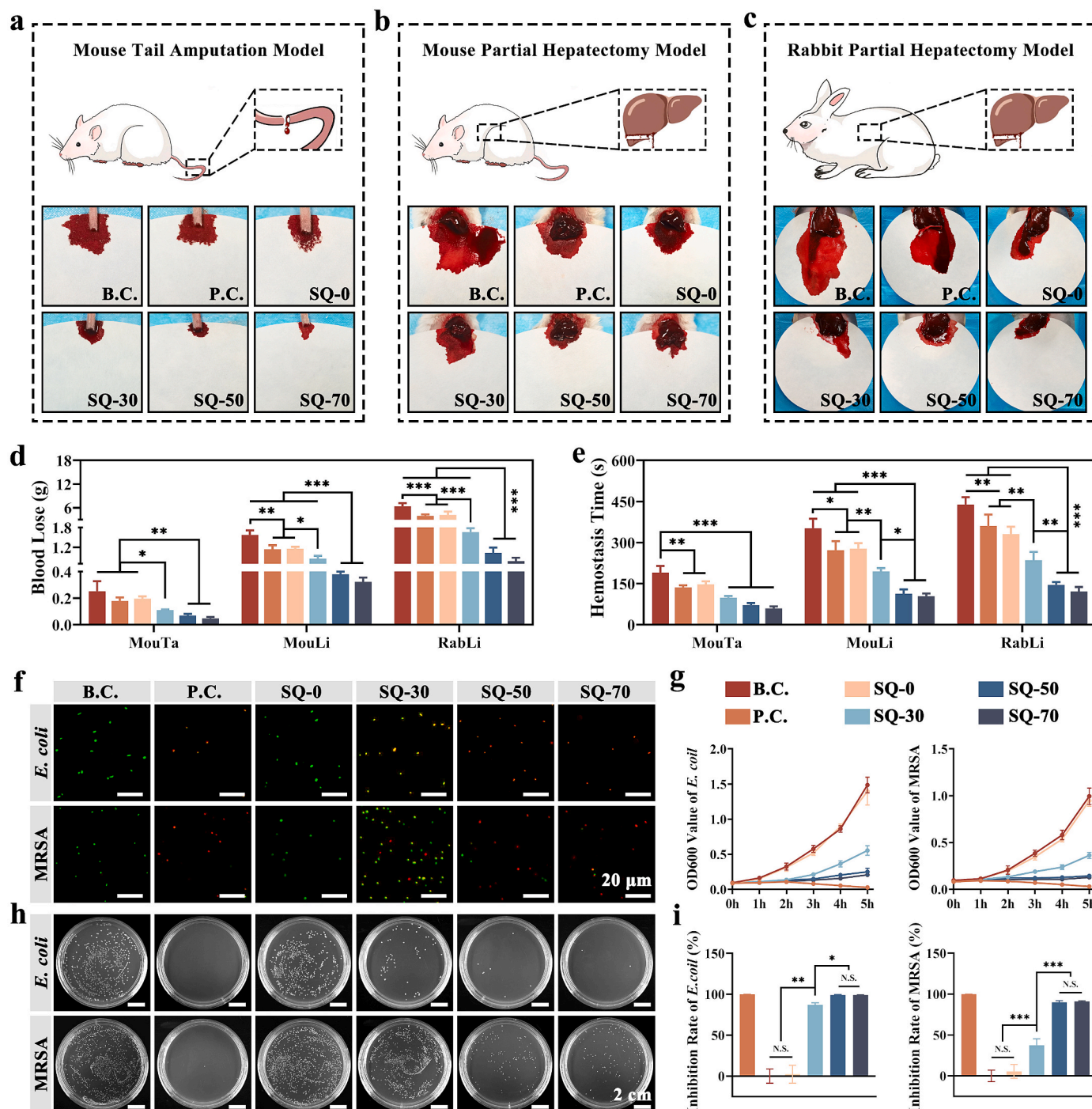
Fig. 2. Hemostatic and antibacterial performance of SQ-n. (a–c) Schematic diagram and physical observation images of three hemostasis animal models. (d–e) Quantitative statistics of blood loss and hemostasis time (n = 3). (f) Live/dead bacterial staining assay for *E. coli* and MRSA. Live bacteria were stained green, dead bacteria were stained red, while bacteria in the intermediate damage state were stained orange (green and red co-stained). (g) The curves proliferation of *E. coli* and MRSA. (h–i) Representative images of surviving *E. coli* and MRSA on culture plates and inhibition rate. Scale bar: 20 μm and 2 cm. (For interpretation of the references to color in this figure legend, the reader is referred to the Web version of this article.)

L929 proliferation similar to that in the B.C. group. However, after 3 days of co-culture, the proliferation of L929 cells in the SQ-70 group was lower than in the other groups, indicating that excessive QC was not conducive to cell proliferation.

Therefore, combining the results of the hemostatic, antibacterial, and biocompatibility assessments, SQ-50 and SQ-70 showed similar excellent hemostatic and antibacterial properties, but considering that the higher QC in SQ-70 was potentially cytotoxicity and detrimental to cell proliferation, SQ-50 was selected for subsequent studies.

3.3. Preparation and characterization of SQAP

Subsequently, based on SQ-50, SQA, and SQAP were prepared to tackle the clinical challenge of anti-tumor recurrence after HCC surgical resection, respectively. Firstly, we tested the degradation performance of BPNSs. As shown in Fig. 3a, the color of BPNSs aqueous dispersion in the sample bottle gradually lightened, and the absorbance value also decreased with time. Quantitative data analysis in Fig. 3b shows that on day 14, BPNSs aqueous dispersion degrades about 57.03 ± 4.33%,

indicating good degradability. The chemical composition of SQA and SQAP was analyzed. As displayed by FTIR in Fig. 3c, BPNSs exhibited two major absorption peaks at 1249 and 1068 cm^{-1} originating from the P=O and P–O vibrations, respectively, which are due to the slight oxidation of the BPNSs surface to generate PO_x^{3-} [47,48]. For AL3818, the two C–O of the ether bond vibrate telescopically at 1020 and 1081 cm^{-1}, respectively; the benzene ring skeleton vibrates to generate three absorption peaks of different intensities at 1425-1623 cm^{-1}; the two absorption peaks from the methyl and methylene vibrations at 2904 and 2947 cm^{-1}; the cyclopropane group vibrates telescopically at 3290 cm^{-1} to generate strong and two strong absorption peaks at 3352 and 3402 cm^{-1} for the primary and secondary amine groups, respectively. The FTIR spectra of SQA and SQAP showed characteristic peaks of AL3818 or/and BPNSs (Fig. 3d). Raman spectra (Fig. 3e) were also used to characterize the raw materials and cryogels. Among them, BPNSs had three characteristic peaks at 364, 440, and 467 cm^{-1} for the out-of-plane phonon mode (A^1g) and two in-plane modes (B_{2g} and A_g^2) [49], respectively. AL3818 had two characteristic peak populations in the 788-1460 cm^{-1} and 2905-2988 cm^{-1}, the former was attributed to carbon-fluorine bonding, ether bonding, and aromatic backbone vibrations, and the latter was attributed to the C–H bond stretching vibration. As shown in Fig. 3f, The SQA showed an enhancement of peak intensity at the position of the characteristic peaks of AL3818 based on the spectra of the SQ-50, and the characteristic peaks of BPNSs further appeared in the Raman spectra of the SQAP. These results supported the successful preparation of SQA and SQAP.

The apparent morphologies of SQA and SQAP were observed by SEM. As shown in Fig. 3g, with the introduction of AL3818 and BPNSs, the surfaces of SQA and SQAP became rougher, and the pore size further decreased. Moreover, the AL3818 and BPNSs components in SQAP were detected by EDS mapping (Fig. 3h and i). Nitrogen (N, 0.62%) and fluorine (F, 0.08%), as characteristic elements of AL3818, and phosphorus (P, 0.05%), as the characteristic element of BPNSs, were uniformly distributed in the SQAP, further confirming the successful loading of AL3818 and BPNSs.

The mechanical properties of SQ-n, SQA, and SQAP were analyzed by compression test. As shown in Fig. 3j and k, the compressive strength of SQ-n gradually decreased at 80% strain with increasing QC content. The compressive strength of SQA, SQAP, and SQ-50 was similar, indicating that the addition of AL3818 and BPNSs did not significantly affect the compressive strength. These results showed that the compressive strength of all groups was above 0.15 MPa, which could meet the clinical requirements for the mechanical properties of biomaterials.

3.4. Photothermal conversion performance and drug release from SQAP

The introduction of BPNSs endowed the cryogels with excellent photothermal conversion performance. Considering the satisfactory anti-tumor effect of mPTT while protecting surrounding normal tissues, SQA and SQAP were irradiated by 808 nm NIR with 0.5 and 0.8 W/cm^2 to evaluate the photothermal conversion performance, respectively. Real-time temperatures were monitored, and representative photothermal images were displayed in Fig. 4a. As shown in Fig. 4b, under 808 nm NIR with 0.5 and 0.8 W/cm^2, the temperatures of SQA were both only slightly elevated at 27.73 ± 0.49 °C and 28.70 ± 1.20 °C, respectively. In contrast, the temperature of SQAP gradually increased to 38.17 ± 0.91 °C under the 0.5 W/cm^2 NIR irradiation and rapidly increased to 45.53 ± 2.30 °C under the 0.8 W/cm^2 NIR irradiation. To achieve the inactivation of tumor cells by mPTT (42–48 °C), 0.8 W/cm^2 was chosen as the optimal NIR power for subsequent experiments. As for the stability of the photothermal conversion performance of SQAP (Fig. 4c), SQAP was exposed to NIR irradiation for more than four cycles and could still reach a temperature of about 45.5 °C within 2 min after the fourth cycle.

The drug release behavior of the cryogels was evaluated. At RT, SQA and SQAP exhibited similar cumulative release of AL3818, reaching 57.59 ± 4.71% and 60.12 ± 4.57% at 14 days, respectively (Fig. 4d). To

evaluate the effect of NIR and the auxiliary effect of BPNSs on the release of AL3818 from SQA and SQAP, the release of AL3818 was examined at different NIR with powers. Under the NIR with 0.5 W/cm^2 irradiation, the cumulative release of AL3818 from SQA was 62.41 ± 4.10%, while that from SQAP increased to 73.65 ± 5.04% (Fig. 4e), indicating that the photothermal conversion of BPNSs promoted the release of AL3818. Moreover, the cumulative release of AL3818 from SQAP reached 85.37 ± 5.26% at 14 d under the NIR with 0.8 W/cm^2 irradiation, achieving a sufficient drug release for the short and long term. As shown in Fig. 4f, it can be seen from either of the drug release curves that the drug release rate of SQAP was significantly increased in a short period under a single NIR irradiation (10 min) and decreased after the withdrawal of NIR. The effect of controlled drug release in a short period was more significant under the NIR with 0.8 W/cm^2 irradiation than that under the NIR with 0.5 W/cm^2 irradiation. This may be attributed to the fact that the higher temperature under the NIR with 0.8 W/cm^2 irradiation made the substance movement more intense and thus promoted the release of AL3818. This photothermal responsive controlled drug release enables "on-demand" drug delivery and reduces the occurrence of drug adverse events and potential drug resistance.

3.5. In vitro evaluation of the anti-angiogenesis effect

To meet the need for continued proliferation, tumors obtain adequate nutrition through new angiogenesis [50]. Therefore, anti-angiogenesis is an important strategy for anti-tumor recurrence. HUVECs were used to evaluate the in vitro anti-angiogenesis effect. As shown in Fig. 5a, unlike the B.C. group, several dead cells (red) appeared in the SQA and SQAP groups, and the morphology of the cells was slightly altered. The cell viability of the SQA and SQAP groups was similar but significantly lower than those of the B.C. group. Fig. 5b and Fig. S5a presented the proliferation of HUVECs, and the SQAP + NIR group showed lower cell proliferation compared to the other groups at 1, 2, and 3 days. Apoptosis of HUVECs was analyzed by flow cytometry (Fig. 5c, Fig. S5b), and the results revealed that the percentage of early apoptosis and late apoptosis of HUVECs in the SQAP + NIR group was 13.23 ± 1.75% and 13.70 ± 1.93%, respectively, which was the most significant compared to those in the other groups.

Subsequently, the scratch assay and Tanswell assay were used to evaluate the migration ability of HUVECs. As shown in Fig. 5d and Fig. S6, compared to the B.C. group (77.57 ± 7.00% and 182.33 ± 20.98), both the SQA and SQAP groups exhibited a larger wound gap area and fewer migrating HUVECs per field (39.07 ± 11.30% and 34.44 ± 11.30%; 115.00 ± 11.79 and 102.67 ± 17.47), respectively, while the SQAP + NIR group was the most significant compared to the other groups (3.92 ± 4.05% and 16.33 ± 14.98), implying that the SQAP could effectively inhibit the migration of HUVECs under NIR irradiation. To evaluate the anti-angiogenesis of SQA and SQAP, a tube formation assay was conducted on HUVECs. As shown in Fig. 5e, compared with other groups, the SQAP + NIR group showed less mature and intact tubular structures, and the branch points and capillary length were significantly decreased (Fig. S7a-b). Moreover, the CD31 MFI (Fig. 5f) was reduced in the SQA and SQAP groups compared to that in the B.C. group. Still, it was the lowest in the SQAP + NIR group, further demonstrating the excellent inhibition of angiogenesis by the SQAP with NIR irradiation (Fig. S7c).

3.6. In vitro evaluation of H22 cells killing effect

Considering the excellent photothermal conversion performance of SQAP and the photothermal responsive controlled release of molecular targeting agent AL3818, H22 cells were used to evaluate their synergistic antitumor effect of mPTT and molecular targeted therapy in vitro. The results of the live/dead cell staining assay (Fig. 6a) showed no red dead cells in the B.C. group, and the viability of H22 cells was 99.23 ± 0.79 %. In contrast, as shown in Fig. S8a, the SQAP + NIR group showed
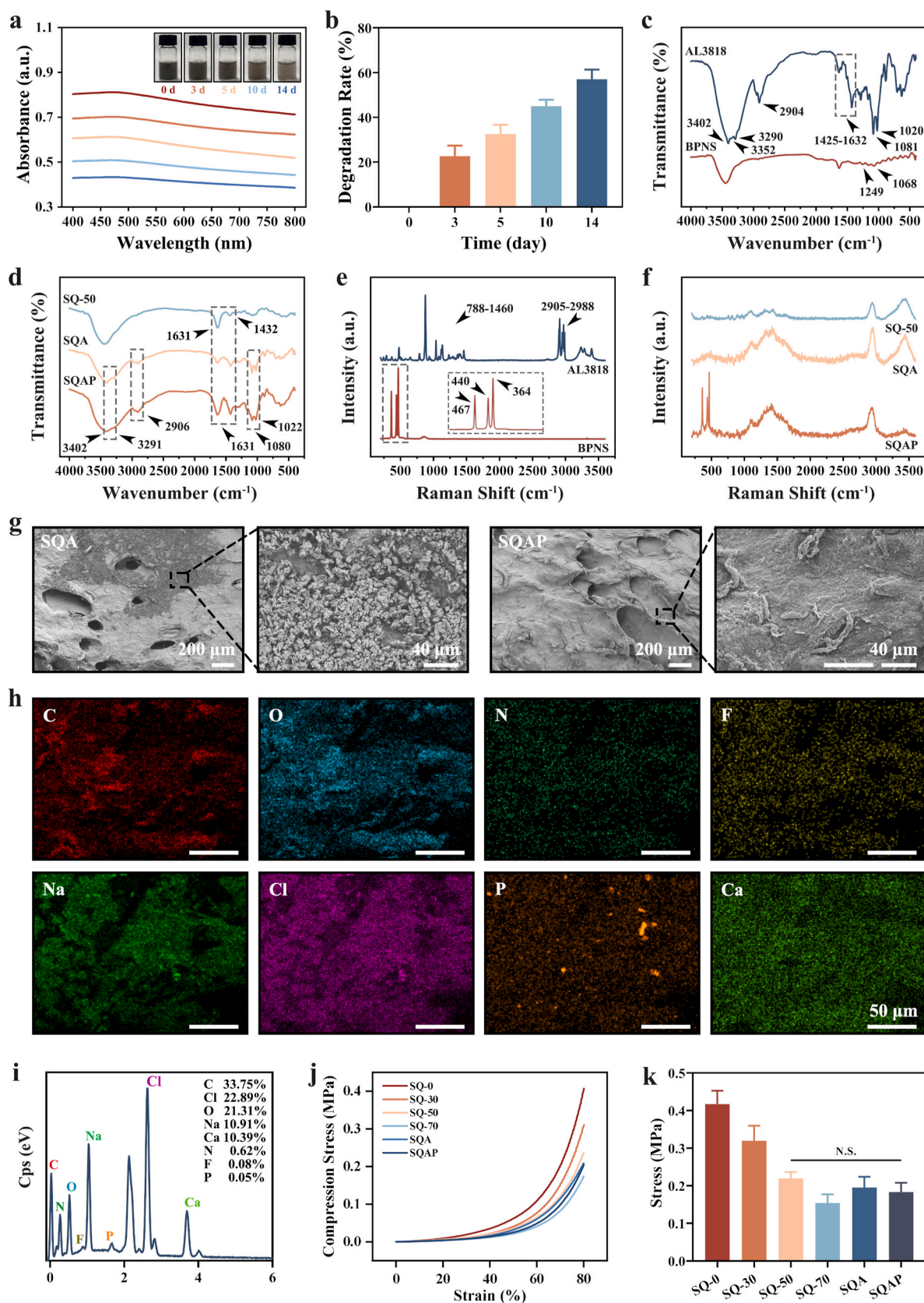
Fig. 3. Preparation and physicochemical characterization of SQA and SQAP. (a) Photographs and UV absorption spectra of BPNSs aqueous dispersions at different time points (days 0, 3, 5, 10, and 14). (b) Quantitative data analysis of the degradation rate of BPNSs aqueous dispersions. (c–d) FTIR and (e–f) Raman spectroscopy of AL3818 and BPNSs raw materials, SQ-50, SQA, and SQAP. (g) SEM images of SQA and SQAP. (h–i) EDS mapping of SQAP. (j) The strain–stress curve of cryogels during the compression test. (k) The quantitative statistical diagram of stress at 80% strain. Scale bar: 40 μm, 50 μm, and 200 μm.
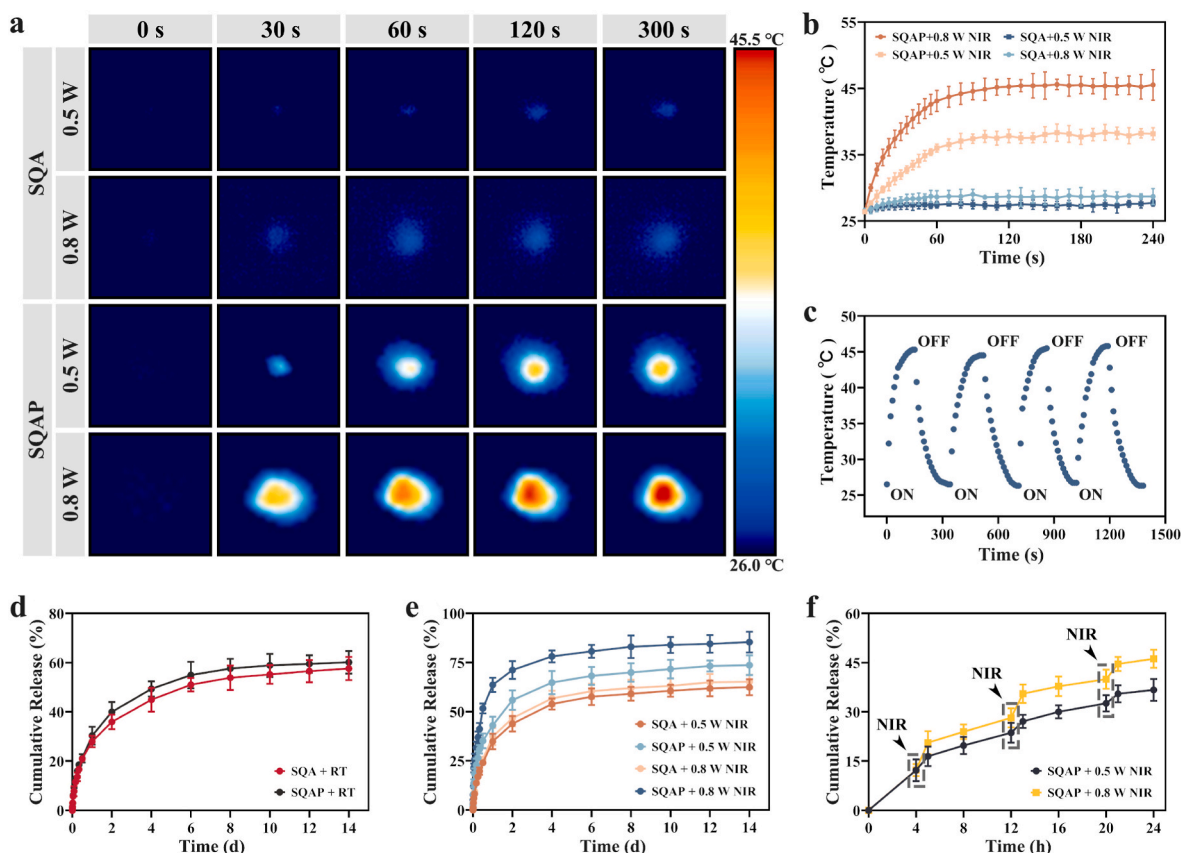
Fig. 4. (a) Representative infrared thermal images of SQA and SQAP under the NIR with 0.5 and 0.8 W/cm^2 irradiation at 0, 30, 60, 120, and 240 s, respectively. (b) The temperature of SQA and SQAP under the NIR with 0.5 and 0.8 W/cm^2 irradiation. (c) The temperature of SQAP during four on/off cycles under the NIR with 0.8 W/cm^2 irradiation. (d–e) The cumulative releasing of AL3818 from SQA and SQAP at RT and under the NIR with 0.5 and 0.8 W/cm^2 irradiation. (f) Sequential multi-photothermal responsive release of AL3818 from SQAP under the NIR with 0.5 and 0.8 W/cm^2 irradiation.

massive red dead cells, and the cell viability was the lowest than that in the other groups and reduced to 51.10 ± 4.80%. CCK8 assay was further used to reflect the proliferative capacity of H22 cells. In Fig. 6b, the proliferation level of H22 cells in the SQA, SQAP, and SQP + NIR groups gradually decreased in similarity with time increasing, while the SQAP + NIR group showed the best inhibition of tumor proliferation. The apoptotic status of H22 cells detected by flow cytometry (Fig. 6c) revealed that the SQAP + NIR group could significantly promote apoptosis of H22 cells, compared to the B.C. group with 0.85 ± 0.41 % early apoptotic cells and 0.11 ± 0.07 % late apoptotic cells (Fig. S8b). In general, the 3′-OH ends resulting from DNA strand breaks during apoptosis can be labeled by the TUNEL method. As shown in Fig. 6d, the SQAP + NIR group had the highest TUNEL MFI than the other groups (Fig. 6g), which aligns with the apoptosis assay results.

In addition, the migration capacity of H22 cells was assessed by scratch assay. As shown in Fig. 6e, the migration area decreased from 91.03 ± 7.67 % in the B.C. group to 50.31 ± 12.45 %, 43.28 ± 4.31 % and 25.78 ± 6.84 % in the SQA, SQAP, and SQP + NIR groups, and further to 8.11 ± 5.30 % in the SQAP + NIR group (Fig. 6h). In Fig. 6f and i, the number of invasive cells in the SQAP + NIR group was significantly lower than those in the other groups. Overall, the synergistic antitumor effect of mPTT and molecular targeted therapy (Fig. 6j) can effectively inhibit the proliferation, migration, and invasion of H22 cells, which is beneficial for inhibiting tumor recurrence and metastasis after surgical resection of HCC.

3.7. SQAP prevents the recurrence after ectopic HCC surgical resection in vivo

Based on the ideal results of the above *in vitro* validation experiments, an *in vivo* mouse model of ectopic HCC was established and further validated the practical applications of SQAP as shown in Fig. 7a BALB/c mice with H22 tumors were randomly divided into four groups: B.C, AL3818, SQAP, and SQAP + NIR groups. The intraoperative hemostatic effect of SQAP was first evaluated; as shown in Fig. 7b, the intraoperative blood loss of mice with SQAP (60.83 ± 12.53 mg) was significantly lower than those with untreated and even lower than those with commercial gauze and gelatin sponge (GS). These results indicated that SQAP could effectively control intraoperative bleeding, thus significantly reducing the risk of death due to massive blood loss and hematogenous metastasis of cancer cells. In Fig. 7c-d, the local temperature of the implanted SQAP rapidly increased to 45.50 ± 1.05 °C under the NIR with 0.8 W/cm^2 irradiation, providing a guarantee for the treatment of mPTT.

The body weight curves of the mice (Fig. 7e) indicated that the mice in the B.C. group showed a decrease in body weights, which was attributed to the deleterious effects of tumor progression on their physiological health; In contrast, the body weights of mice in the other groups were broadly stable and maintained at normal levels without significant differences, suggesting that early and effective therapeutic interventions can improve the physical condition of mice. The dynamic curve of tumor volume (Fig. 7f-g) showed that all 5 mice in the SQAP + NIR group survived with the smallest recurrent tumor volume (55.76 ± 22.36 mm^3) compared to the other groups. Due to the tumor recurrence resulting in mice death, until day 21, 3 mice remained in the B.C. group, 4 mice remained in both AL3818 and SQAP groups. At the same time, all
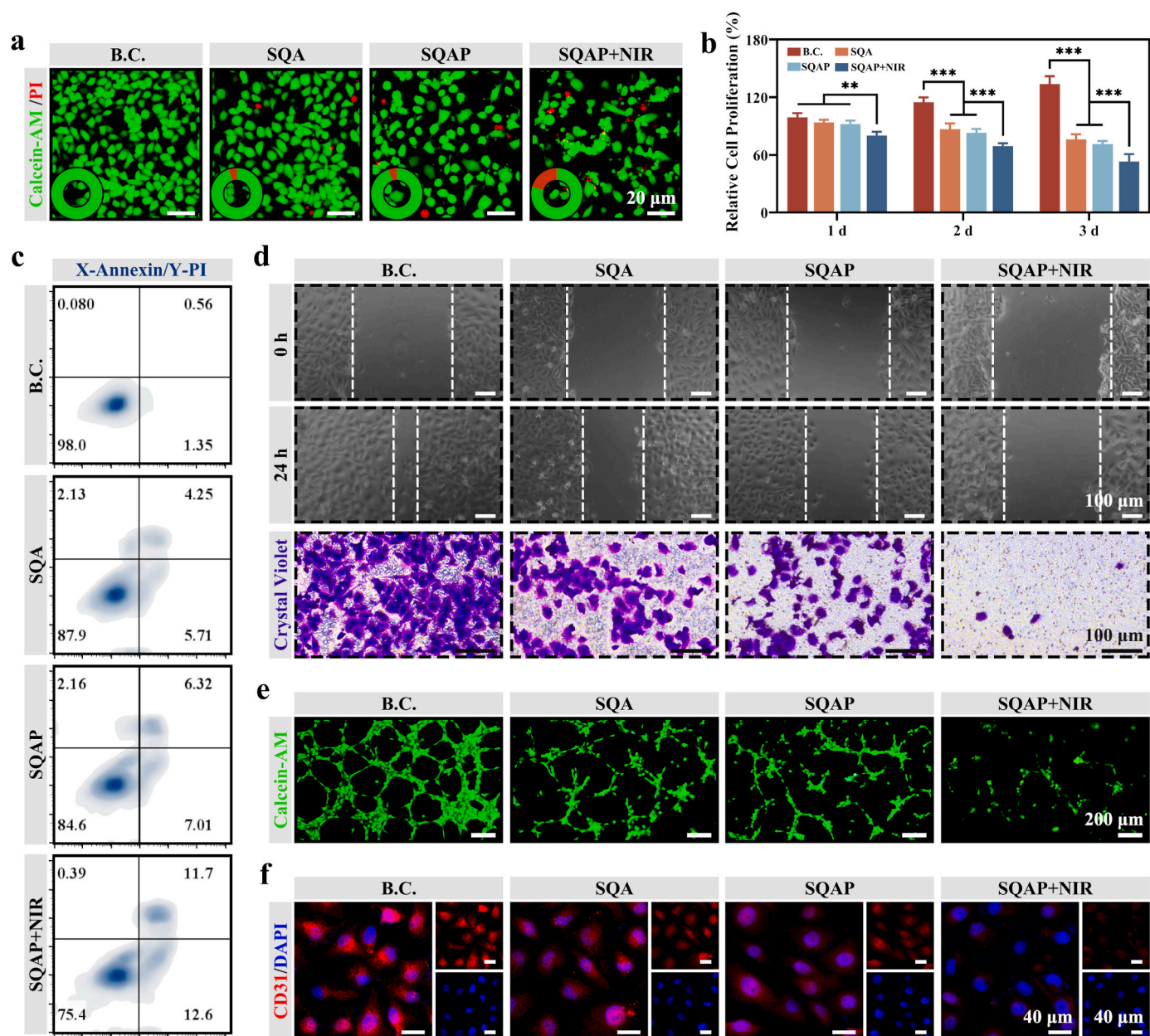
Fig. 5. In vitro evaluation of anti-angiogenesis effect. (a) Representative images of live/dead cell staining assay for HUVECs in different groups. (b) Relative proliferation rates of HUVECs in different groups. (c) Representative flow cytometry profiles (Annexin V-AbFluor™ 488/PI staining) upon varied treatments. (d) Representative images of scratch assay and Transwell assay, respectively. (e) Representative images of a tube formation assay (Calcein-AM staining). (f) Representative images of CD31 immunofluorescence staining. Scale bar: 20 μm, 40 μm, 100 μm, and 200 μm. Significant differences are denoted by **$P < 0.01$ and ***$P < 0.001$.

mice in the SQAP + NIR group survived (Fig. 7h). Fig. 7i also revealed that with the extension of time, the B.C. group had the largest weight of recurrent tumor tissues, followed by AL3818, SQAP, and SQAP + NIR groups. As shown in Fig. 7j, the survival analysis of 40 days observed in each group suggested that mice in the SQAP + NIR group had the most extended overall survival and the best prognosis. Moreover, ultrasound and color Doppler were used to assess the sizes and the vascular component of the recurrent tumor, respectively. Fig. 7k detected that recurrent tumor sizes were consistent with the results of recurrent tumor volume curves. For the Color Doppler images, angiogenesis in recurrent tumors was the least in the SQAP + NIR group. In conclusion, SQAP provided excellent intraoperative hemostasis, which could effectively inhibit tumor recurrence and angiogenesis in combination with molecular targeted therapy and mPTT assisted by NIR.

3.8. Histological evaluation of locally recurrent tumors and distant liver metastases

Finally, a histological evaluation of the isolated tumor tissue was performed. As shown in Fig. 8a, the tumor cells in the B.C. group were diffusely distributed, exhibiting significant tumor heterogeneity with pathological nuclear schizophrenia, a high proportion of Ki67-positive cells, and a low proportion of TUNEL-positive cells. However, the proportion of Ki67-positive cells and the proportion of TUNEL-positive cells in the SQAP + NIR group were significantly downregulated and upregulated, respectively (Fig. 8b-c). These results indicate that the NIR-assisted SQAP could inhibit tumor proliferation, promote tumor necrosis and apoptosis, and thereby suppress local tumor recurrence after resection. Fig. 8d displayed the immunofluorescence stainings of CD31
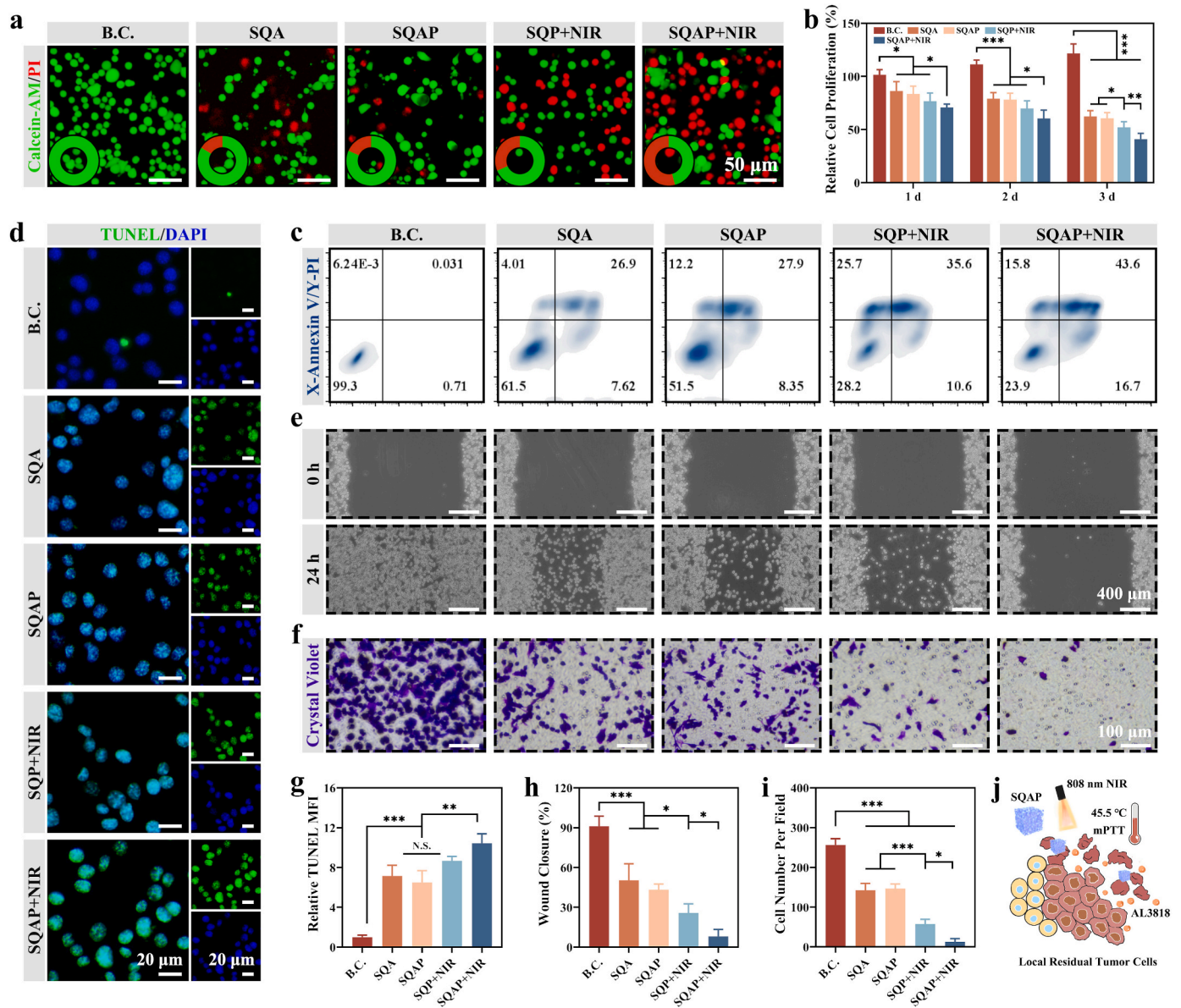
Fig. 6. *In vitro* evaluation of H22 cells killing effect. (a) Representative images of live/dead cell staining assay for H22 cells in the B.C., SQA, SQAP, SQP + NIR, and SQAP + NIR, respectively. (b) Relative proliferation rates of H22 cells. (c) Representative flow cytometry profiles (Annexin V-AbFluor™ 488/PI staining) upon varied treatments. (d) Representative images of TUNEL immunofluorescence staining. (e) Representative images of the scratch assay. (f) Representative images of Transwell assay. (g) Relative mean fluorescence intensity (MFI) of TUNEL for H22 cells. (h–i) Quantitative results of the scratch assay and Tanswell assay. (j) Diagram of SQAP in action through mPTT and AL3818. Scale bar: 20 μm, 50 μm, 100 μm, and 400 μm. Significant differences are denoted by $*P < 0.05$, $**P < 0.01$, and $***P < 0.001$.

and HIF-1α. HIF-1α reflects the level of hypoxia in tumor tissues and is a core regulator of angiogenesis under hypoxia, and its upregulated expression can stimulate tumor angiogenesis [51]. The expression levels of CD31 and HIF-1α were the lowest in the SQAP + NIR group (Fig. S9). Considering that VEGF, a downstream molecule of HIF-1α, VEGF plays a vital role in the angiogenesis of HCC, the expression level of VEGF in recurrent tumor tissues was assessed by immunohistochemical staining analysis (Fig. S10). Similarly, quantitative analysis showed a significant decrease in VEGF positive stained area in the SQAP + NIR group compared to the other groups (Fig. 8e). These histological evaluation results may be attributed to the ability of NIR-assisted SQAP to release large amounts of AL3818 *in situ*, targeting VEGF and thus inhibiting tumor angiogenesis; in addition, NIR-assisted SQAP may also reduce tumor oxygen demand by inhibiting tumor proliferation, thereby downregulating HIF-1α production, and blocking the expression of the downstream molecule VEGF and its further pro-angiogenesis effects.

Previous studies have reported that mPTT produced thermal damage to tumor cells while triggering tumor immunity [52,53]. Therefore, the induction of tumor immunity by NIR-assisted SQAP was examined by using the immunohistochemistry of the pro-inflammatory factor IL-6 and the immunosuppressive factor IL-10 (Fig. 8f). The SQAP + NIR group supported more expression of IL-6 and lower expression of IL-10 than other groups, indicating the role of NIR-assisted SQAP in enhancing tumor immunity (Fig. S11).

Biosafety is particularly important for the *in vivo* application of biomaterials. Organ tissue samples (heart, liver, spleen, lung, and kidney) and fresh plasma were collected for histological and biochemical analyses, respectively. The H&E staining showed no differences between the experimental and B.C. groups in multiple organs (Fig. S12). In addition, the H&E staining results of the *in vivo* degradation experiment (Fig. S13) of SQAP showed disintegration and separation on day 7, and some aggregates were still present on day 14. On day 28, most of the
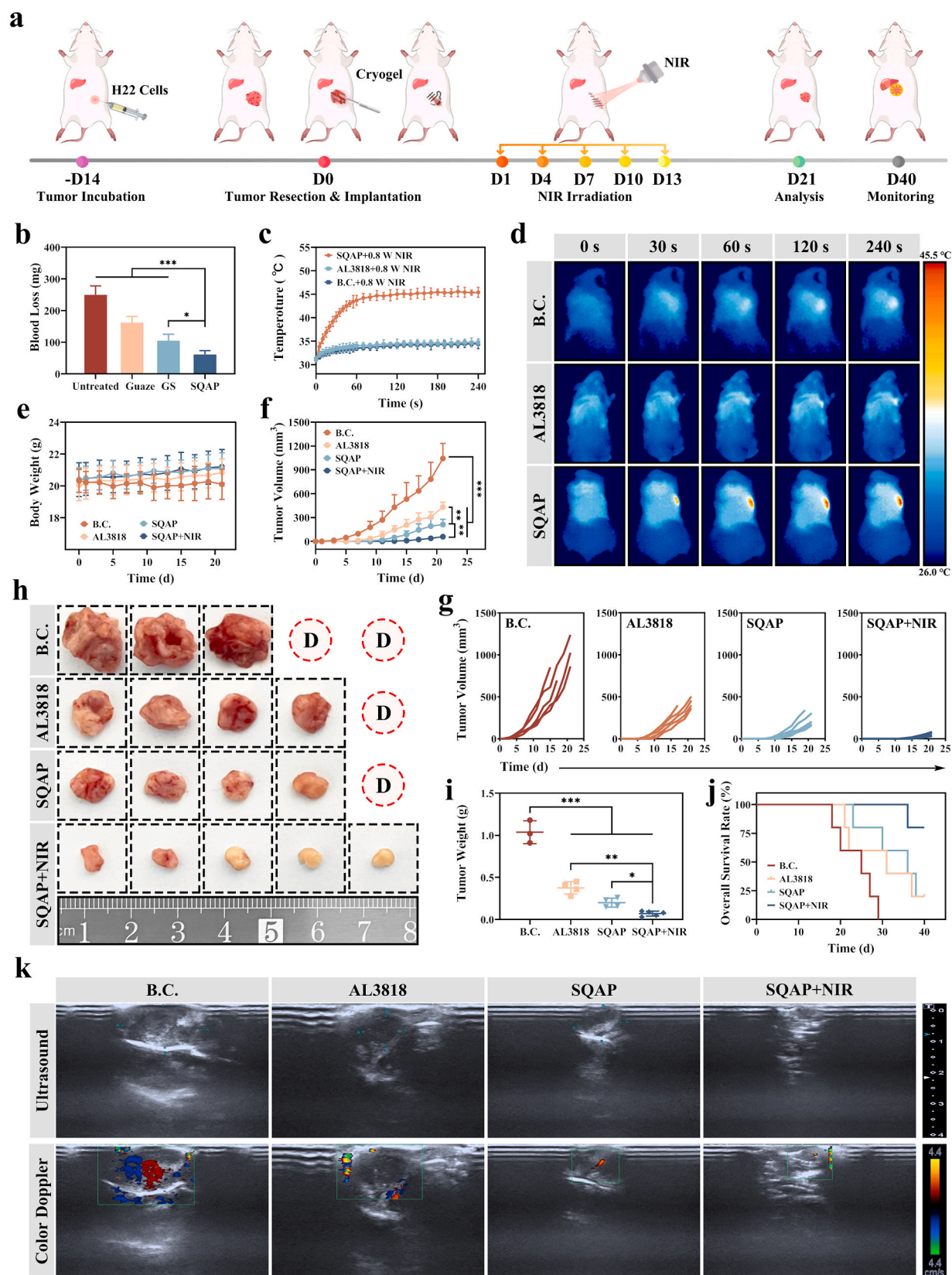
Fig. 7. *In vivo* hemostasis and prevention of recurrence after xenograft HCC surgical resection. (a) The process timeline of animal model for xenograft HCC surgical resection. (b) Quantitative statistics of intraoperative blood loss. (c–d) Temperature elevation curves of tumor resection site and infrared thermal images. (e–i) Body weight, tumor volume, and tumor weight evolution within 21 days. (j) Overall survival curve for mice in different groups within 40 days. (k) Representative ultrasound and color Doppler images on day 21. The red and blue represented the presence of blood flow, with red representing blood flow toward the ultrasound probe and blue representing blood flow back toward the ultrasound probe. Significant differences are denoted by *$P < 0.05$, **$P < 0.01$, and ***$P < 0.001$. (For interpretation of the references to color in this figure legend, the reader is referred to the Web version of this article.)
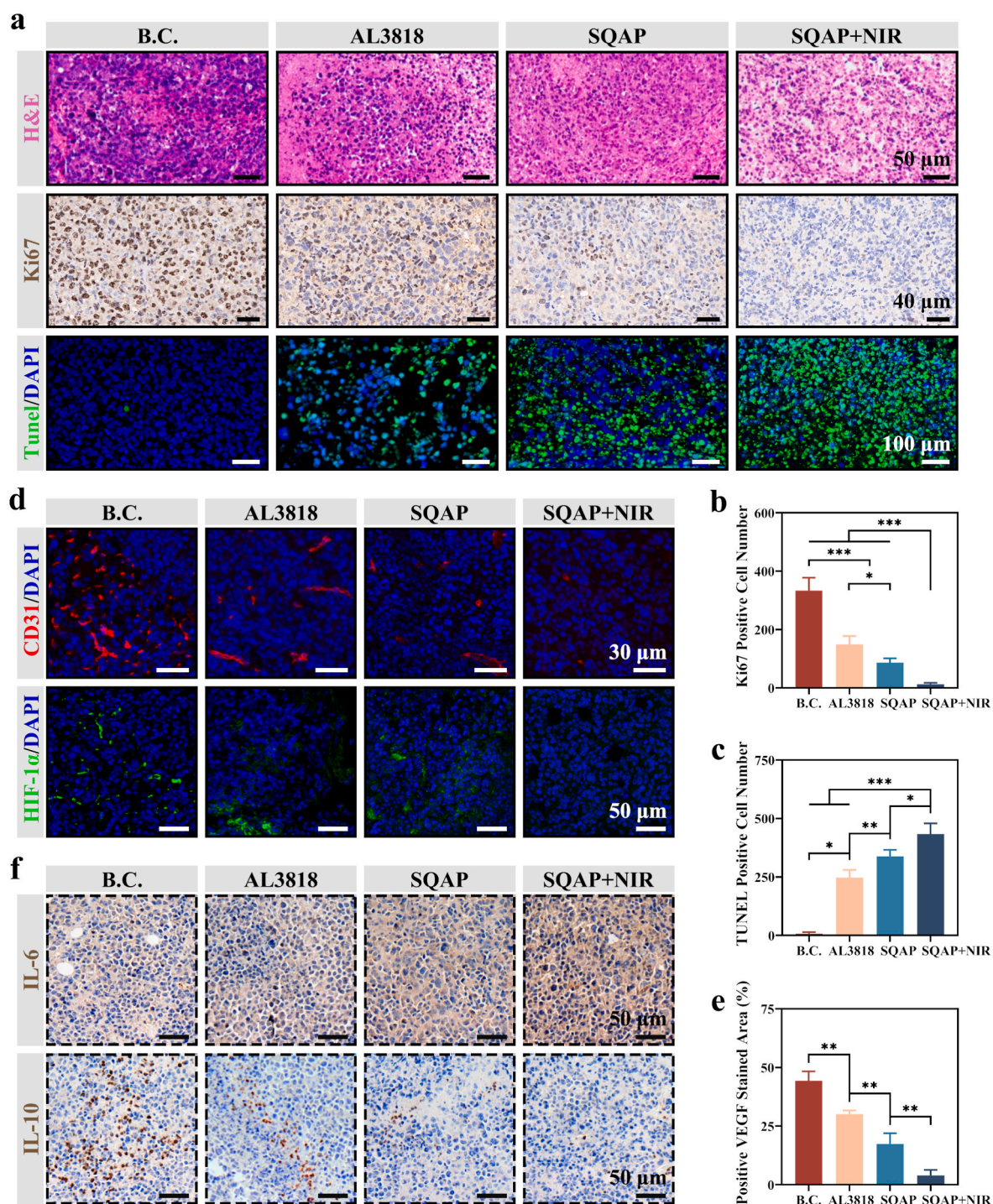
Fig. 8. Histological evaluation of locally recurrent tumors. (a) Representative images of H&E staining, Ki67 immunohistochemical staining, and TUNEL immuno-fluorescence staining images. (b) Quantitative analysis of Ki67 positive cell number. (c) Quantitative analysis of TUNEL positive cell number. (d) Representative images of CD31 and HIF-1α immunofluorescence staining. (e) Quantitative analysis of VEGF positive stained area. (f) Representative images of IL-6 and IL-10 immunohistochemical staining. Scale bar: 30 μm, 40 μm, 50 μm, and 100 μm. Significantly different: $*P < 0.05$, $**P < 0.01$, and $***P < 0.001$.

SQAP degraded, and the remaining thin strips of debris were surrounded by surrounding normal tissue. This shows that SQAP has good biocompatibility and provides a reference for determining the therapeutic window of NIR irradiation.

4. Discussion

Residual tumor recurrence after HCC surgical resection, strongly associated with poorer clinical outcomes and overall survival, remains a considerable challenge in clinical practice [54]. Recently, various nanomaterials with photothermal conversion [55], photodynamic properties [56,57], enzyme catalysis [58], and immunomodulation [59] have attracted widespread attention and have been applied to antitumor therapy. However, most studies [60–62] on anti-tumor recurrence focus on the inactivation of postoperative residual micro infiltrative tumor cells, which is undoubtedly essential. It is worth noting that intraoperative bleeding and postoperative infection debilitate patient immunity and are also risk factors for postoperative tumor recurrence. In this work,

NIR-assisted SQAP with hemostatic, antibacterial, anti-angiogenesis, and anti-tumor were rationally designed and developed as a "one-stop" strategy to address clinical needs. Specifically, this multifunctional SQAP not only effectively reduces intraoperative blood loss and the risk of postoperative bacterial infection through QC but also inhibits local tumor recurrence and potential distant metastasis through BPNSs-based photo-thermal conversion and the photothermal responsive release of AL3818 exerting synergistic mPTT and molecular targeting therapy.

Compared with previous findings in the same animal model using sonodynamic therapy [51] or nanovaccine [62] to treat postoperative tumor recurrence, our NIR-assisted SQAP exhibited a faster or similar tumor inhibitory rate. Considering its effective treatment, our cryogels can be applied to translational and regenerative medicine. Given the limitations of rodent models, we will further test our multifunctional cryogels in large animals and optimize the properties accordingly for higher clinical translational value.

5. Conclusions

In summary, we first prepared a series of SQ-n by SA and QC electrostatic interactions. Based on the composition of QC, SQ-50 exhibited superior hemostatic and antibacterial effects along with great cytocompatibility *in vitro*. AL3818 and BPNSs were then introduced into SQ-50 to prepare SQAP successfully. Specifically, through the photothermal conversion properties of BPNSs and the molecular targeted therapeutic effects of AL3818, the multifunctional SQAP could generate mPTT with photothermal responsive controlled release of AL3818 and exhibited excellent inhibition of angiogenesis and tumor proliferation *in vitro*. *In vivo* ectopic HCC surgical resection mouse model further demonstrated that NIR-assisted SQAP could inhibit local tumor recurrence and potential distant metastasis. This novel "one-stop" strategy suggests a new direction for intraoperative and postoperative interventions of HCC surgical resection.

Yiming Liu: Investigation, Data curation, Writing – original draft, Chuan Tian: Investigation, Data curation, Methodology, Chengzhi Zhang: Investigation, Formal analysis, Zaoqu Liu: Investigation, Jing Li: Formal analysis, Yahua Li: Formal analysis, Quanhui Zhang: Formal analysis, Shengnan Ma: Methodology, Supervision, Dechao Jiao: Supervision, Xinwei Han: Visualization, Supervision, Funding acquisition, Yanan Zhao: Conceptualization, Writing – review & editing, Supervision, Funding acquisition.

Ethics approval

All animal experiments were approved by the Animal Care and Use Committee of the First Affiliated Hospital of Zhengzhou University and carried out in strict compliance with the National Research Council's Guide for the Care and Use of Laboratory Animals.

Declaration of competing interest

The authors declare that they have no known competing financial interests or personal relationships that could have appeared to influence the work reported in this paper.

Data availability

Data will be made available on request.

Acknowledgments

Appendix A. Supplementary data

Supplementary data to this article can be found online at https://doi.org/10.1016/j.mtbio.2023.100746.

References

[1] J.M. Llovet, R.K. Kelley, A. Villanueva, A.G. Singal, E. Pikarsky, S. Roayaie, R. Lencioni, K. Koike, J. Zucman-Rossi, R.S. Finn, Hepatocellular carcinoma, Nat Rev Dis Primers 7 (2021) 6, https://doi.org/10.1038/s41572-020-00240-3.
[2] Y. Sugawara, T. Hibi, Surgical treatment of hepatocellular carcinoma, Biosci Trends 15 (2021) 138–141, https://doi.org/10.5582/bst.2021.01094.
[3] D. Wang, X. Zheng, B. Fu, Z. Nian, Y. Qian, R. Sun, Z. Tian, H. Wei, Hepatectomy promotes recurrence of liver cancer by enhancing IL-11-STAT3 signaling, EBioMedicine 46 (2019) 119–132, https://doi.org/10.1016/j.ebiom.2019.07.058.
[4] A. Villanueva, Hepatocellular carcinoma, N. Engl. J. Med. 380 (2019) 1450–1462, https://doi.org/10.1056/NEJMra1713263.
[5] M. Abu Hilal, T. Underwood, M.G. Taylor, K. Hamdan, H. Elberm, N.W. Pearce, Bleeding and hemostasis in laparoscopic liver surgery, Surg. Endosc. 24 (2010) 572–577, https://doi.org/10.1007/s00464-009-0597-x.
[6] S.C. Katz, J. Shia, K.H. Liau, M. Gonen, L. Ruo, W.R. Jarnagin, Y. Fong, M.I. D'Angelica, L.H. Blumgart, R.P. Dematteo, Operative blood loss independently predicts recurrence and survival after resection of hepatocellular carcinoma, Ann. Surg. 249 (2009) 617–623, https://doi.org/10.1097/SLA.0b013e31819ed22f.
[7] T. Wei, X.F. Zhang, F. Bagante, F. Ratti, H.P. Marques, S. Silva, O. Soubrane, V. Lam, G.A. Poultsides, I. Popescu, R. Grigorie, S. Alexandrescu, G. Martel, A. Workneh, A. Guglielmi, T. Hugh, L. Aldrighetti, I. Endo, T.M. Pawlik, Postoperative infectious complications Worsen long-term survival after curative-intent resection for hepatocellular carcinoma, Ann. Surg Oncol. 29 (2022) 315–324, https://doi.org/10.1245/s10434-021-10565-2.
[8] T. Yang, K. Liu, C.F. Liu, Q. Zhong, J. Zhang, J.J. Yu, L. Liang, C. Li, M.D. Wang, Z.L. Li, H. Wu, H. Xing, J. Han, W.Y. Lau, Y.Y. Zeng, Y.H. Zhou, W.M. Gu, H. Wang, T. H. Chen, Y.M. Zhang, W.G. Zhang, T.M. Pawlik, M.C. Wu, F. Shen, Impact of postoperative infective complications on long-term survival after liver resection for hepatocellular carcinoma, Br. J. Surg. 106 (2019) 1228–1236, https://doi.org/10.1002/bjs.11231.
[9] A.W.H. Chan, J. Zhong, S. Berhane, H. Toyoda, A. Cucchetti, K. Shi, T. Tada, C.C. N. Chong, B.D. Xiang, L.Q. Li, P.B.S. Lai, V. Mazzaferro, M. Garcia-Finana, M. Kudo, T. Kumada, S. Roayaie, P.J. Johnson, Development of pre and post-operative models to predict early recurrence of hepatocellular carcinoma after surgical resection, J. Hepatol. 69 (2018) 1284–1293, https://doi.org/10.1016/j.jhep.2018.08.027.
[10] P. Tabrizian, G. Jibara, B. Shrager, M. Schwartz, S. Roayaie, Recurrence of hepatocellular cancer after resection: patterns, treatments, and prognosis, Ann. Surg. 261 (2015) 947–955, https://doi.org/10.1097/SLA.0000000000000710.
[11] Y. Wu, Y. Yao, J. Zhang, H. Gui, J. Liu, J. Liu, Tumor-targeted injectable double-network hydrogel for prevention of breast cancer recurrence and wound infection via synergistic photothermal and brachytherapy, Adv. Sci. 9 (2022), e2200681, https://doi.org/10.1002/advs.202200681.
[12] D.M. Manas, J. Figueras, D. Azoulay, J.C. Garcia Valdecasas, J. French, E. Dixon, N. O'Rourke, N. Grovale, V. Mazzaferro, Expert opinion on advanced techniques for hemostasis in liver surgery, Eur. J. Surg. Oncol. 42 (2016) 1597–1607, https://doi.org/10.1016/j.ejso.2016.05.008.
[13] Z. Wang, W. You, W. Wang, W. Tian, F. Chen, Y. Xiao, Y. Chen, X. Wang, Dihydromyricetin-Incorporated Multilayer Nanofibers Accelerate Chronic Wound Healing by Remodeling the Harsh Wound Microenvironment, Advanced Fiber Materials 4 (2022) 71–1556, https://doi.org/10.1007/s42765-022-00180-5.
[14] S. Lv, M. Cai, F. Leng, X. Jiang, Biodegradable carboxymethyl chitin-based hemostatic sponges with high strength and shape memory for non-compressible hemorrhage, Carbohydr. Polym. 288 (2022), 119369, https://doi.org/10.1016/j.carbpol.2022.119369.
[15] V.M. Gun'ko, I.N. Savina, S.V. Mikhalovsky, Cryogels: morphological, structural and adsorption characterisation, Adv. Colloid Interface Sci. 187–188 (2013) 1–46, https://doi.org/10.1016/j.cis.2012.11.001.
[16] E.I. Bektas, G. Gurel Pekozer, F.N. Kok, G. Torun Kose, Evaluation of natural gum-based cryogels for soft tissue engineering, Carbohydr. Polym. 271 (2021), 118407, https://doi.org/10.1016/j.carbpol.2021.118407.
[17] N.M. Sanchez-Ballester, B. Bataille, I. Soularol, Sodium alginate and alginic acid as pharmaceutical excipients for tablet formulation: structure-function relationship, Carbohydr. Polym. 270 (2021), 118399, https://doi.org/10.1016/j.carbpol.2021.118399.
[18] F. Wang, J. Sun, J. Shi, J. Zhou, X. Ma, X. Song, X. Su, L. Liu, Multifunctionalized alginate/polydopamine cryogel for hemostasis, antibacteria and promotion of wound healing, Int. J. Biol. Macromol. 224 (2023) 1373–1381, https://doi.org/10.1016/j.ijbiomac.2022.10.223.
[19] Y. Zhao, C. Tian, Y. Liu, Z. Liu, J. Li, Z. Wang, X. Han, All-in-one bioactive properties of photothermal nanofibers for accelerating diabetic wound healing, Biomaterials 295 (2023), 122029, https://doi.org/10.1016/j.biomaterials.2023.122029.
[20] P.L. Bedard, D.M. Hyman, M.S. Davids, L.L. Siu, Small molecules, big impact: 20 years of targeted therapy in oncology, Lancet 395 (2020) 1078–1088, https://doi.org/10.1016/S0140-6736(20)30164-1.
[21] C. Le Tourneau, J.P. Delord, A. Goncalves, C. Gavoille, C. Dubot, N. Isambert, M. Campone, O. Tredan, M.A. Massiani, C. Mauborgne, S. Armanet, N. Servant,

I. Bieche, V. Bernard, D. Gentien, P. Jezequel, V. Attignon, S. Boyault, A. Vincent-Salomon, V. Servois, M.P. Sablin, M. Kamal, X. Paoletti, S. investigators, Molecularly targeted therapy based on tumour molecular profiling versus conventional therapy for advanced cancer (SHIVA): a multicentre, open-label, proof-of-concept, randomised, controlled phase 2 trial, Lancet Oncol. 16 (2015) 1324–1334, https://doi.org/10.1016/S1470-2045(15)00188-6.

[22] C. He, T. Wu, Y. Hao, Anlotinib induces hepatocellular carcinoma apoptosis and inhibits proliferation via Erk and Akt pathway, Biochem. Biophys. Res. Commun. 503 (2018) 3093–3099, https://doi.org/10.1016/j.bbrc.2018.08.098.

[23] A.X. Zhu, D.G. Duda, D.V. Sahani, R.K. Jain, HCC and angiogenesis: possible targets and future directions, Nat. Rev. Clin. Oncol. 8 (2011) 292–301, https://doi.org/10.1038/nrclinonc.2011.30.

[24] F. Song, B. Hu, J.W. Cheng, Y.F. Sun, K.Q. Zhou, P.X. Wang, W. Guo, J. Zhou, J. Fan, Z. Chen, X.R. Yang, Anlotinib suppresses tumor progression by blocking the VEGFR2/PI3K/AKT cascade in intrahepatic cholangiocarcinoma, Cell Death Dis. 11 (2020) 573, https://doi.org/10.1038/s41419-020-02749-7.

[25] G. Shen, F. Zheng, D. Ren, F. Du, Q. Dong, Z. Wang, F. Zhao, R. Ahmad, J. Zhao, Anlotinib: a novel multi-targeting tyrosine kinase inhibitor in clinical development, J. Hematol. Oncol. 11 (2018) 120, https://doi.org/10.1186/s13045-018-0664-7.

[26] Y. Sun, A. Zhou, W. Zhang, Z. Jiang, B. Chen, J. Zhao, Z. Li, L. Wang, X. Bi, H. Zhao, K. Liu, Anlotinib in the treatment of advanced hepatocellular carcinoma: an open-label phase II study (ALTER-0802 study), Hepatol Int 15 (2021) 621–629, https://doi.org/10.1007/s12072-021-10171-0.

[27] X. Yi, Q.Y. Duan, F.G. Wu, Low-temperature photothermal therapy: strategies and applications, Research (2021), 9816594, https://doi.org/10.34133/2021/9816594, 2021.

[28] Z. Jiang, T. Li, H. Cheng, F. Zhang, X. Yang, S. Wang, J. Zhou, Y. Ding, Nanomedicine potentiates mild photothermal therapy for tumor ablation, Asian J. Pharm. Sci. 16 (2021) 738–761, https://doi.org/10.1016/j.ajps.2021.10.001.

[29] C. Zhan, Y. Huang, G. Lin, S. Huang, F. Zeng, S. Wu, A gold nanocage/cluster hybrid structure for whole-body multispectral optoacoustic tomography imaging, EGFR inhibitor delivery, and photothermal therapy, Small 15 (2019), e1900309, https://doi.org/10.1002/smll.201900309.

[30] G. Gao, Y.W. Jiang, H.R. Jia, W. Sun, Y. Guo, X.W. Yu, X. Liu, F.G. Wu, From perinuclear to intranuclear localization: a cell-penetrating peptide modification strategy to modulate cancer cell migration under mild laser irradiation and improve photothermal therapeutic performance, Biomaterials 223 (2019) 119443, https://doi.org/10.1016/j.biomaterials.2019.119443.

[31] J. Liu, S. Smith, C. Wang, Reversing the epithelial-mesenchymal transition in metastatic cancer cells using cd146-targeted black phosphorus nanosheets and a mild photothermal treatment, ACS Nano 16 (2022) 3208–3220, https://doi.org/10.1021/acsnano.1c11070.

[32] Y. Li, R. Fu, Z. Duan, C. Zhu, D. Fan, Artificial nonenzymatic antioxidant MXene nanosheet-anchored injectable hydrogel as a mild photothermal-controlled oxygen release platform for diabetic wound healing, ACS Nano 16 (2022) 7486–7502, https://doi.org/10.1021/acsnano.1c10575.

[33] J.R. Choi, K.W. Yong, J.Y. Choi, A. Nilghaz, Y. Lin, J. Xu, X. Lu, Black phosphorus and its biomedical applications, Theranostics 8 (2018) 1005–1026, https://doi.org/10.7150/thno.22573.

[34] L. Qin, S. Jiang, H. He, G. Ling, P. Zhang, Functional black phosphorus nanosheets for cancer therapy, J Control Release 318 (2020) 50–66, https://doi.org/10.1016/j.jconrel.2019.12.013.

[35] Z. Li, C. Tian, D. Jiao, J. Li, Y. Li, X. Zhou, H. Zhao, Y. Zhao, X. Han, Synergistic effects of silver nanoparticles and cisplatin in combating inflammation and hyperplasia of airway stents, Bioact. Mater. 9 (2022) 266–280, https://doi.org/10.1016/j.bioactmat.2021.07.029.

[36] K. Chen, H. Pan, Z. Yan, Y. Li, D. Ji, K. Yun, Y. Su, D. Liu, W. Pan, A novel alginate/gelatin sponge combined with curcumin-loaded electrospun fibers for postoperative rapid hemostasis and prevention of tumor recurrence, Int. J. Biol. Macromol. 182 (2021) 1339–1350, https://doi.org/10.1016/j.ijbiomac.2021.05.074.

[37] A. Wan, Q. Xu, Y. Sun, H. Li, Antioxidant activity of high molecular weight chitosan and N,O-quaternized chitosans, J. Agric. Food Chem. 61 (2013) 6921–6928, https://doi.org/10.1021/jf402242e.

[38] X. Yin, H. Xie, R. Li, S. Yan, H. Yin, Regulating association strength between quaternary ammonium chitosan and sodium alginate via hydration, Carbohydr. Polym. 255 (2021), 117390, https://doi.org/10.1016/j.carbpol.2020.117390.

[39] T.J. Jayeoye, T. Rujiralai, Green, in situ fabrication of silver/poly(3-aminophenyl boronic acid)/sodium alginate nanogel and hydrogen peroxide sensing capacity, Carbohydr. Polym. 246 (2020) 116657, https://doi.org/10.1016/j.carbpol.2020.116657.

[40] P. Han, Z. Li, X. Wei, L. Tang, M. Li, Z. Liang, X. Yin, S. Wei, Ion-imprinted thermosensitive chitosan derivative for heavy metal remediation, Carbohydr. Polym. 248 (2020) 116732, https://doi.org/10.1016/j.carbpol.2020.116732.

[41] Y. Zhao, A. Xiao, P. Wu, F. Chen, Q. Zhang, X. Liang, X. Han, X. Shi, Y. Li, Y. Chen, Fabrication of hydroxypropyl chitosan/soy protein isolate hydrogel for effective hemorrhage control, Tissue Eng Part A 27 (2021) 788–795, https://doi.org/10.1089/ten.TEA.2020.0174.

[42] X. Zhao, H. Wu, B. Guo, R. Dong, Y. Qiu, P.X. Ma, Antibacterial anti-oxidant electroactive injectable hydrogel as self-healing wound dressing with hemostasis and adhesiveness for cutaneous wound healing, Biomaterials 122 (2017) 34–47, https://doi.org/10.1016/j.biomaterials.2017.01.011.

[43] Y. Liang, Z. Li, Y. Huang, R. Yu, B. Guo, Dual-dynamic-bond cross-linked antibacterial adhesive hydrogel sealants with on-demand removability for post-wound-closure and infected wound healing, ACS Nano 15 (2021) 7078–7093, https://doi.org/10.1021/acsnano.1c00204.

[44] Y.C. Chung, Y.P. Su, C.C. Chen, G. Jia, H.L. Wang, J.C. Wu, J.G. Lin, Relationship between antibacterial activity of chitosan and surface characteristics of cell wall, Acta Pharmacol. Sin. 25 (2004) 932–936.

[45] H. Tan, R. Ma, C. Lin, Z. Liu, T. Tang, Quaternized chitosan as an antimicrobial agent: antimicrobial activity, mechanism of action and biomedical applications in orthopedics, Int. J. Mol. Sci. 14 (2013) 1854–1869, https://doi.org/10.3390/ijms14011854.

[46] P. Mao, P. Peng, Z. Liu, Z. Xue, C. Yao, Risk factors and clinical outcomes of hospital-acquired MRSA infections in chongqing, China, Infect. Drug Resist. 12 (2019) 3709–3717, https://doi.org/10.2147/IDR.S223536.

[47] Z. Sofer, J. Luxa, D. Bousa, D. Sedmidubsky, P. Lazar, T. Hartman, H. Hardtdegen, M. Pumera, The covalent functionalization of layered black phosphorus by nucleophilic reagents, Angew Chem. Int. Ed. Engl. 56 (2017) 9891–9896, https://doi.org/10.1002/anie.201705722.

[48] C. Xie, L. Wang, Y. Liu, M. Chen, P. Du, Y. Wang, X. Ma, S. Yang, Fullerene covalent passivation of black phosphorus nanosheets toward enhanced near-infrared-II photothermal therapy, ACS Appl. Mater. Interfaces 15 (2023) 20686–20696, https://doi.org/10.1021/acsami.3c01074.

[49] B. Yang, J. Yin, J. Chen, S. Pan, H. Yao, Y. Gao, J. Shi, 2D-Black-Phosphorus-Reinforced 3D-printed scaffolds:A stepwise countermeasure for osteosarcoma, Adv Mater 30 (2018), https://doi.org/10.1002/adma.201705611.

[50] C. Viallard, B. Larrivee, Tumor angiogenesis and vascular normalization: alternative therapeutic targets, Angiogenesis 20 (2017) 409–426, https://doi.org/10.1007/s10456-017-9562-9.

[51] Y. Liang, M. Li, Y. Huang, B. Guo, An integrated strategy for rapid hemostasis during tumor resection and prevention of postoperative tumor recurrence of hepatocellular carcinoma by antibacterial shape memory cryogel, Small 17 (2021), e2101356, https://doi.org/10.1002/smll.202101356.

[52] Y. Lu, F. Wu, Y. Xu, C. He, S. Luo, X. Sun, Triple functional mild photothermal improves gene editing of PD-L1 for enhanced antitumor immunity, J Control Release 354 (2023) 57–68, https://doi.org/10.1016/j.jconrel.2022.12.052.

[53] H. Tang, X. Xu, Y. Chen, H. Xin, T. Wan, B. Li, H. Pan, D. Li, Y. Ping, Reprogramming the tumor microenvironment through second-near-infrared-window photothermal genome editing of PD-L1 mediated by supramolecular gold nanorods for enhanced cancer immunotherapy, Adv Mater 33 (2021), e2006003, https://doi.org/10.1002/adma.202006003.

[54] F. Milana, M.A. Polidoro, S. Famularo, A. Lleo, R. Boldorini, M. Donadon, G. Torzilli, Surgical strategies for recurrent hepatocellular carcinoma after resection: a review of current evidence, Cancers 15 (2023), https://doi.org/10.3390/cancers15020508.

[55] D. Xi, M. Xiao, J. Cao, L. Zhao, N. Xu, S. Long, J. Fan, K. Shao, W. Sun, X. Yan, X. Peng, NIR light-driving barrier-free group rotation in nanoparticles with an 88.3% photothermal conversion efficiency for photothermal therapy, Adv Mater 32 (2020), e1907855, https://doi.org/10.1002/adma.201907855.

[56] D. Xi, N. Xu, X. Xia, C. Shi, X. Li, D. Wang, S. Long, J. Fan, W. Sun, X. Peng, Strong π-π stacking stabilized nanophotosensitizers: improving tumor retention for enhanced therapy for large tumors in mice, Adv Mater 34 (2022), e2106797, https://doi.org/10.1002/adma.202106797.

[57] G. He, M. He, R. Wang, X. Li, H. Hu, D. Wang, Z. Wang, Y. Lu, N. Xu, J. Du, J. Fan, X. Peng, W. Sun, A near-infrared light-activated photocage based on a ruthenium complex for cancer phototherapy, Angew Chem. Int. Ed. Engl. 62 (2023), e202218768, https://doi.org/10.1002/anie.202218768.

[58] Y. Guo, Y. Fan, Z. Wang, G. Li, M. Zhan, J. Gong, J.P. Majoral, X. Shi, M. Shen, Chemotherapy mediated by biomimetic polymeric nanoparticles potentiates enhanced tumor immunotherapy via amplification of endoplasmic reticulum stress and mitochondrial dysfunction, Adv Mater 34 (2022), e2206861, https://doi.org/10.1002/adma.202206861.

[59] F. Ding, F. Li, D. Tang, B. Wang, J. Liu, X. Mao, J. Yin, H. Xiao, J. Wang, Z. Liu, Restoration of the immunogenicity of tumor cells for enhanced cancer therapy via nanoparticle-mediated copper chaperone inhibition, Angew Chem. Int. Ed. Engl. 61 (2022), e202203546, https://doi.org/10.1002/anie.202203546.

[60] B. Li, X. Zhang, Z. Wu, T. Chu, Z. Yang, S. Xu, S. Wu, Y. Qie, Z. Lu, F. Qi, M. Hu, G. Zhao, J. Wei, Y. Zhao, G. Nie, H. Meng, R. Liu, S. Li, Reducing postoperative recurrence of early-stage hepatocellular carcinoma by a wound-targeted nanodrug, Adv. Sci. 9 (2022), e2200477, https://doi.org/10.1002/advs.202200477.

[61] Y. Gao, J. Wang, H. Han, H. Xiao, W.K. Jin, S. Wang, S. Shao, Z. Wang, W. Yang, L. Wang, L. Weng, A nanoparticle-containing polycaprolactone implant for combating post-resection breast cancer recurrence, Nanoscale 13 (2021) 14417–14425, https://doi.org/10.1039/d1nr04125h.

[62] S. Zhang, Y. Feng, M. Meng, Z. Li, H. Li, L. Lin, C. Xu, J. Chen, K. Hao, Z. Tang, H. Tian, X. Chen, A generally minimalist strategy of constructing biomineralized high-efficiency personalized nanovaccine combined with immune checkpoint blockade for cancer immunotherapy, Biomaterials 289 (2022), 121794, https://doi.org/10.1016/j.biomaterials.2022.121794.